Lithos 170-171 (2013) 117–143

Contents lists available at SciVerse ScienceDirect

Lithos

journal homepage: www.elsevier.com/locate/lithos

Ultra-high temperature granulite-facies metamorphic rocks from the Mozambique belt of SW Tanzania

H. Sommer [a,*], A. Kröner [a,b]

[a] Institut für Geowissenschaften, Universität Mainz, D-55099 Mainz, Germany
[b] Beijing SHRIMP Centre, Institute of Geology, Chinese Academy of Geological Sciences, 26 Baiwanzhuang Road, 100037 Beijing, China

ARTICLE INFO

Article history:
Received 1 October 2012
Accepted 20 February 2013
Available online 1 March 2013

Keywords:
Tanzania
Granulite
Metamorphic petrology
P–T-Path
Zircon geochronology

ABSTRACT

The metamorphic rocks in the Neoproterozoic (Pan-African) Mozambique belt of southwestern Tanzania, around the town of Songea, can be subdivided into one- and two pyroxene bearing charnockitic gneisses, migmatitic granitoid gneisses and amphibolite-facies metapelites. Lower-grade amphibolite-facies rocks are rare and can be classified as sillimanite- and/or garnet-bearing metapelites. Most of the studied charnockitic gneisses show excellent corona textures with large orthopyroxene grains rimmed by clinopyroxene, followed by quartz and well developed garnet rims due to the reaction Opx + Pl = Grt + Cpx + Qtz that formed during isobaric cooling. These and other charnockitic gneisses show symplectites of orthopyroxene and An-rich plagioclase that resulted from the breakdown of garnet during isothermal decompression due to the reaction Grt + Cpx + Qtz = Opx + Pl. Geothermobarometric calculations yield up to ~1050 °C and up to ~12 kbar for peak metamorphic conditions. These are higher temperature and slightly lower pressure conditions than reported for other granulite-facies terrains in the Mozambique belt of Tanzania. Single zircon Pb–Pb evaporation and U-Pb SHRIMP ages for magmatic zircons extracted from two charnockitic and two granitic gneisses cluster in two groups, one at ~750 Ma and one at ~1150 Ma with the older reflecting the time of emplacement of the igneous precursors, and the younger approximating the time of charnockitization. These protolith ages are similar to those farther east in the Masasi area of southern Tanzania, as well as in northern Mozambique and in southern Malawi, and suggest that the Mozambique belt consists of chronologically heterogeneous assemblages whose pre-metamorphic tectonic setting remains obscure.

© 2013 Elsevier B.V. All rights reserved.

1. Introduction

The Neoproterozoic high-grade terrains of the Mozambique belt (MB; Holmes, 1951) in East Africa and Madagascar, together with the lower grade Arabian-Nubian Shield of NE Africa and Arabia, make up the East African Orogen (EAO; Johnson et al., 2011; Stern, 1994). Several authors discussed the southern continuation of the EAO into East Antarctica, and the southern extension through India into Antarctica (Collins and Pisarevsky, 2005; Collins and Windley, 2002; Jacobs et al., 1998; Pant et al., 2012).

Shackleton (1986) suggested that the MB is a complex assemblage of Proterozoic belts of different ages and may thus be polyorogenic. Emplacement ages for magmatic precursors of the granulites in the MB range between ~800 and ~2900 Ma from northern, central and southern Tanzania (Fig. 1A; Table 1; Supplement Table 1; De Waele et al., 2006; Kröner et al., 2003; Maboko, 2000; Maboko and Nakamura, 1996; Möller et al., 2000; Muhongo et al., 2001; Sommer et al., 2003, 2005a,b, 2008; Spooner et al., 1970; Thomas et al., 2013), whereas metamorphic zircons and monazite record a major high-grade metamorphic event during the late Neoproterozoic at 620–650 Ma and a second metamorphic event at ~550 Ma (Supplement Table 1, Sommer et al., 2003, 2005b). The granulite-facies rocks of the MB in southwestern Tanzania have not previously been investigated because of their complex metamorphic history and remote location. To reconstruct the metamorphic history of the study area, a combined approach of field mapping, petrology and geochronology was used. We report *P–T* data and single zircon ages for high-grade metamorphic rocks around the town of Songea (Figs. 1A, B) and compare these data with those reported from similar high-grade rocks elsewhere in Tanzania, Mozambique, Malawi, and Madagascar.

2. Geological setting

The MB of Tanzania (Fig. 1A; Table 1) consists of a Neoproterozoic crustal domain that is predominantly composed of granulite- and amphibolite-facies rocks (Appel et al., 1998; Harpum, 1970; Muhongo, 1994, 1999; Pinna, 1995; Quennell et al., 1956; Sommer et al., 2003, 2008). To its west, medium- to high-grade rocks and undeformed granitoids and volcanic rocks of Palaeoproterozoic age make up the

* Corresponding author at: School of Geography, Earth Science and Environment, The University of the South Pacific, Laucala Campus, Suva, Fiji Islands.
E-mail address: info@holgersommer.de (H. Sommer).

0024-4937/$ – see front matter © 2013 Elsevier B.V. All rights reserved.
http://dx.doi.org/10.1016/j.lithos.2013.02.014

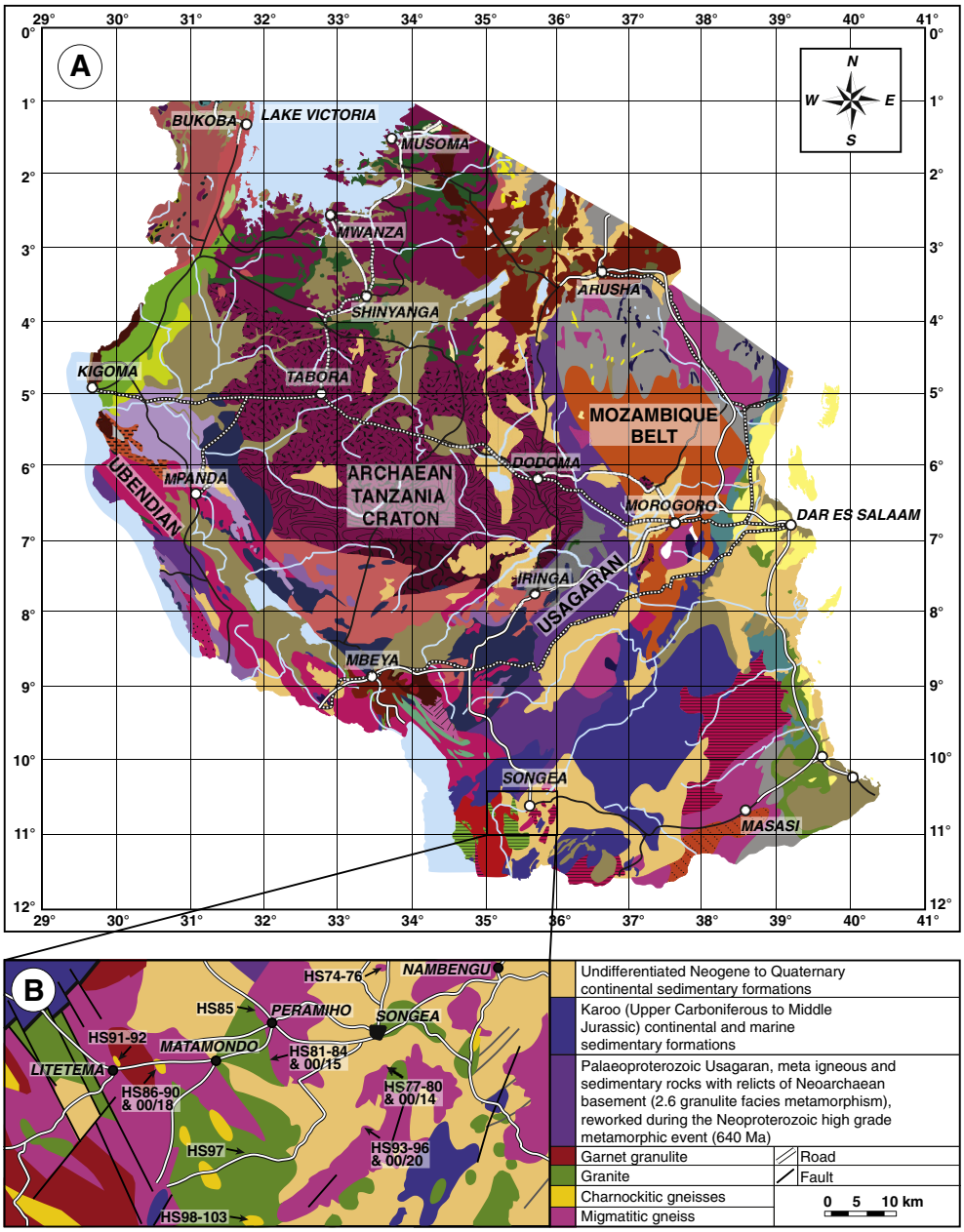

Fig. 1. (A) Geological map of Tanzania showing the main geological terrains: Cenozoic domains, Paleozoic and Mesozoic basins, Neoproterozoic domains, Neoproterozoic Mozambique Belt, Mesoproterozoic belts, Palaeoproterozoic Ubendian and Usagaran belt and Archaean basement (modified after Pinna et al., 2004). (B) Geological overview map of the study around the town of Songea showing major rock units and sample locations. (For interpretation of the references to color in this figure legend, the reader is referred to the web version of this article.)

Ubendian–Usagaran belt that borders the Archaean Tanzania Craton along its southeastern margin (Fig. 1A; Table 1; Collins and Pisarevsky, 2005; Reddy et al., 2003, 2004; Sommer et al., 2005b). The formation of Neoproterozoic high-temperature and high-pressure (HT/HP) rocks in the MB of East Africa and Madagascar has been interpreted as the result of Neoproterozoic terrane amalgamation and collision, characterized by recumbent, isoclinal folds, thrusts, nappe structures, high-temperature ductile strike–slip shear zones and pervasive down-dip stretching lineations (Fritz et al., 2005, 2009; Hepworth, 1972; Muhongo, 1994; Shackleton, 1986, 1993, 1996 and references therein). The age of regional granulite-facies metamorphism is well constrained by zircon U–Pb SHRIMP and Pb–Pb evaporation ages as well as U–Pb monazite ages of around 620–650 Ma (Kröner et al., 2003; Möller et al., 2000; Muhongo et al., 2001; Sommer et al., 2003, 2005a). A summary of previous geochronology on high-grade rocks is given in Supplement Table 1. Granulite-facies rocks in the MB of northern Mozambique, southern Malawi, and Madagascar yielded metamorphic ages between 615 and 550 Ma (Bingen et al., 2009; Kröner, 2001, 2000; Kröner et al., 2001; Thomas et al., 2010). Thus, it is now well documented that two distinct metamorphic event occurred within the MB, one at 620–650 Ma and a second at ~550 Ma. Consequently, both granulite-facies metamorphic events in the MB have been punctuated (Kröner, 2001; Muhongo et al., 2001; Sommer et al., 2003, 2005a).

Much of the Songea area is covered by Karoo and Neogene sediments, which obscure many of the underlying Proterozoic high-grade

Table 1
Detailed description of geological units shown in Fig. 1A.

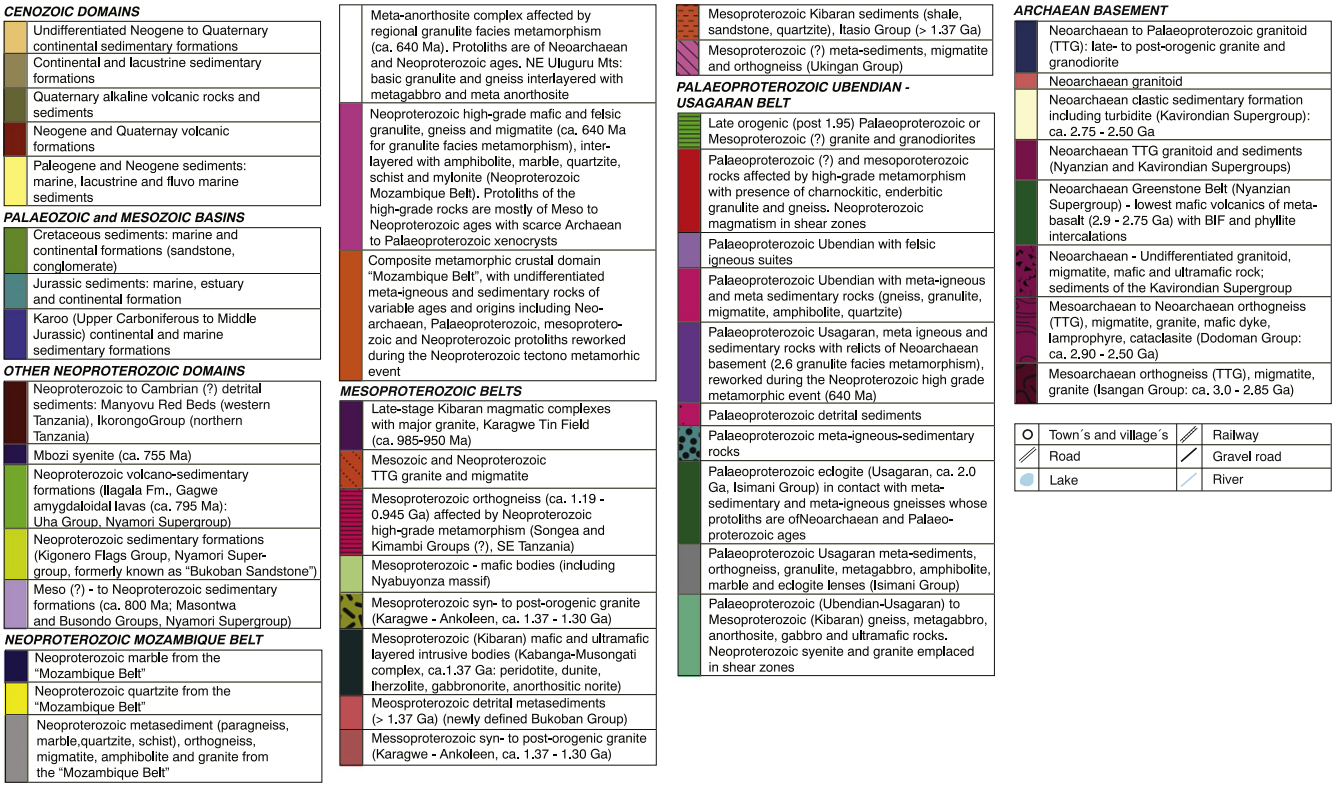

Table 2
Mineral assemblages from the analyzed rocks of the Songea area. Four lithologies were found: metapelites (mp), gneisses (gn), granites (gr) and charnockites (chg).

SAMPLE	Lith.	Qtz	Grt	Opx	Cpx	Am	Pl	Kfs	Bt	Ms	Sil	Spl	Ti-Hem	Ilm	Czo/Ep	Dol	Cal	Other
HS74	mp	x	x			x	x	x	x	x				x	x	x	x	
HS75	mp	x	x			x	x	x	x	x				x	x	x	x	
HS76	mp	x	x			x	x	x	x	x				x	x	x	x	
HS77	gr	x				x	x	x	x									Apatite
HS78	gr	x					x	x	x	x			x					Allanite, graphite
HS79	gr	x					x	x	x	x								
HS80	gr	x					x	x		x			x	x				
HS81	gn	x	x				x	P	x			i		x				
HS81b	gn	x	x				x	P	x				x	x				Melt textures
HS82	gn	x	x				x	x	x		i	i		x				
HS83	chg	x	relic	x + s	x	x	x + s						x	x				Scapolite
HS84	chg	x	c	x + s		x	A + s		x				x	x				
HS86	chg	x		x	x		x							x				
HS87	gn	x					A	P	x									
HS88	chg	x	x + c	x	x + c	x	A	X	x				x	x				Apatite
HS89	chg	x	x + c	x			x	x	x				x	x				
HS90	chg	x	x + c	x	c		x	x	x									
HS91	chg	x		x	x	x	x						x	x				
HS92	chg	x	c	x + s	x		A + s	rims	x				x	x				Apatite
HS93	gn	x				x	x	x	x									
HS94	gn	x				x	x	x	x	x								Allanite
HS95	gn	x						x	x						x			Rutile
HS96	gn	x				x	x	x	x	x								Allanite
HS97	gr	x						x	x									
HS98	gr	x					x	x	x									Apatite
HS99	gn	x				x	x	x	x				x					Sphene
HS100	mp	x	x				x	x	x	(x)	x			x				
HS101	mp	x					x	x	x	(x)	x			x				
HS102	mp	x	x				x	x	x	(x)	x			x				

Lith. = lithology; x = equilibrium phase; c = corona; s = symplectite; A = anitperthite; P = perthite, i = inclusion; () retrograde.

Table 3
Representative EPMA analyses of garnet.

Ideal cations	8.00	8.00	8.00	8.00	8.00	8.00	8.00	8.00	8.00	8.00	8.00	8.00	8.00	8.00	8.00	8.00	8.00	8.00	8.00	8.00	8.00	8.00	8.00	8.00
Ideal oxygens	12	12	12	12	12	12	12	12	12	12	12	12	12	12	12	12	12	12	12	12	12	12	12	12
Sample	HS75	HS75	HS81	HS81	HS81b	HS81b	HS81b	HS82	HS82	HS83	HS84	HS84	HS84	HS88	HS88	HS88	HS90	HS90	HS92	HS92	HS100	HS100	HS102	HS102
	Grt3	Grt11	Grt3	Grt4	Grt16	Grt2	Grt12	Grt11	Grt12	Grt4	Grt18	Grt25	Grt26	Grt1	Grt2	Grt9	Grt1	Grt7	Grt16	Grt20	Grt1	Grt2	Grt1	Grt6
	/	Rim	Core	Rim	Core	Rim	O-Rim	Core	Rim	/	/	Core	Rim	Core	Rim	/	Core	Rim	/	/	Core	Rim	Core	Rim
	poicilitic	poicilitic	/	/	/	/	/	/	/	relic	Corona	Corona	Corona	relic	/	Corona	/	/	Corona	Corona	/	/	/	/
Generation	Gt III	Gt III	Gt I	Gt I	Gt I	Gt I	Gt II	Gt II	Gt II	Gt I	Gt II	Gt II	Gt II	Gt I	Gt II	Gt II	Gt II	Gt II	Gt II	Gt II	Gt III	Gt III	Gt III	Gt III
wt %																								
SiO2	37.21	37.54	39.72	39.28	39.14	39.16	38.73	39.72	38.95	39.60	38.67	38.52	38.34	37.92	38.00	38.59	38.67	38.65	38.15	38.73	37.09	37.04	37.56	36.82
TiO2	0.26	0.07	0.03	0.03	0.02	0.05	0.06	0.00	0.08	0.05	0.02	0.00	0.00	0.10	0.07	0.05	0.04	0.17	0.00	0.69	0.01	0.01	0.01	0.04
Al2O3	20.84	20.72	22.31	21.65	21.37	21.46	21.35	22.07	22.06	21.96	21.79	21.43	21.44	21.06	21.27	21.21	21.31	21.49	21.10	20.69	21.12	21.01	21.16	20.93
Cr2O3	0.00	0.00	0.00	0.00	0.00	0.00	0.00	0.00	0.00	0.00	0.00	0.00	0.00	0.00	0.00	0.00	0.00	0.00	0.02	0.08	0.11	0.04	0.09	0.06
BaO	0.00	0.00	0.00	0.00	0.00	0.00	0.00	0.00	0.00	0.00	0.00	0.00	0.00	0.00	0.00	0.00	0.00	0.00	0.00	0.00	0.00	0.00	0.00	0.00
FeO	28.58	26.57	23.48	23.15	26.06	25.60	24.92	25.42	25.72	24.15	24.85	24.09	23.75	28.73	27.75	27.38	28.01	25.54	24.71	25.47	28.45	28.15	28.87	27.55
MnO	5.08	4.69	0.82	0.66	0.59	0.67	0.63	0.49	0.69	2.21	1.12	1.05	1.11	1.38	1.37	0.70	1.05	0.85	1.98	2.13	9.96	10.77	9.02	11.19
MgO	2.45	3.15	12.32	12.81	9.02	10.63	6.76	11.01	9.32	6.42	6.75	6.11	6.19	4.84	4.59	5.01	7.93	6.80	5.64	5.28	2.27	1.94	3.07	1.99
CaO	5.14	6.60	1.62	1.17	3.88	1.91	7.49	1.33	2.87	7.96	6.65	8.23	8.25	5.20	6.94	7.68	3.17	6.40	7.76	8.02	1.15	0.94	1.24	1.17
Na2O	0.00	0.00	0.00	0.00	0.00	0.00	0.00	0.00	0.00	0.00	0.00	0.00	0.00	0.00	0.00	0.00	0.00	0.00	0.00	0.00	0.00	0.00	0.00	0.00
K2O	0.00	0.00	0.00	0.00	0.00	0.00	0.00	0.00	0.00	0.00	0.00	0.00	0.00	0.00	0.00	0.00	0.00	0.00	0.00	0.00	0.00	0.00	0.00	0.00
Total	**99.56**	**99.34**	**100.30**	**98.75**	**100.08**	**99.48**	**99.94**	**100.04**	**99.69**	**102.35**	**99.85**	**99.43**	**99.08**	**99.23**	**99.99**	**100.11**	**100.18**	**99.90**	**99.36**	**101.09**	**100.16**	**99.90**	**101.02**	**99.75**
Ferric form	**HS74**	**HS75**	**HS81**	**HS81**	**HS81b**	**HS81b**	**HS81b**	**HS82**	**HS82**	**HS83**	**HS84**	**HS84**	**HS84**	**HS88**	**HS88**	**HS88**	**HS90**	**HS90**	**HS92**	**HS92**	**HS100**	**HS100**	**HS102**	**HS102**
Si	3.00	3.00	2.98	2.99	3.00	3.00	3.00	3.02	2.99	3.00	3.00	3.00	2.99	3.01	2.99	3.00	2.99	3.00	2.99	3.00	3.00	3.01	3.00	3.00
Al	1.98	1.95	1.98	1.94	1.93	1.94	1.95	1.98	2.00	1.96	1.99	1.97	1.97	1.97	1.97	1.95	1.94	1.96	1.95	1.89	2.01	2.01	1.99	2.01
Ti	0.02	0.00	0.00	0.00	0.00	0.00	0.00	0.00	0.00	0.00	0.00	0.00	0.00	0.01	0.00	0.00	0.00	0.01	0.00	0.04	0.00	0.00	0.00	0.00
Cr	0.00	0.00	0.00	0.00	0.00	0.00	0.00	0.00	0.00	0.00	0.00	0.00	0.00	0.00	0.00	0.00	0.00	0.00	0.00	0.00	0.01	0.00	0.01	0.00
Ba	0.00	0.00	0.00	0.00	0.00	0.00	0.00	0.00	0.00	0.00	0.00	0.00	0.00	0.00	0.00	0.00	0.00	0.00	0.00	0.00	0.00	0.00	0.00	0.00
Fe3	0.00	0.03	0.05	0.07	0.06	0.05	0.05	0.02	0.00	0.04	0.02	0.03	0.04	0.00	0.05	0.04	0.06	0.02	0.07	0.02	0.00	0.00	0.01	0.00
Mg	0.29	0.38	1.38	1.45	1.03	1.21	0.78	1.25	1.07	0.72	0.78	0.71	0.72	0.57	0.54	0.58	0.92	0.79	0.66	0.61	0.27	0.24	0.37	0.24
Fe	1.93	1.75	1.42	1.40	1.62	1.59	1.56	1.62	1.65	1.49	1.59	1.53	1.51	1.91	1.78	1.74	1.75	1.63	1.55	1.63	1.92	1.91	1.92	1.88
Mn	0.35	0.32	0.05	0.04	0.04	0.04	0.04	0.03	0.04	0.14	0.07	0.07	0.07	0.09	0.09	0.05	0.07	0.06	0.13	0.14	0.68	0.74	0.61	0.77
Ca	0.44	0.57	0.13	0.10	0.32	0.16	0.62	0.11	0.24	0.65	0.55	0.69	0.69	0.44	0.58	0.64	0.26	0.53	0.65	0.67	0.10	0.08	0.11	0.10
Na	0.00	0.00	0.00	0.00	0.00	0.00	0.00	0.00	0.00	0.00	0.00	0.00	0.00	0.00	0.00	0.00	0.00	0.00	0.00	0.00	0.00	0.00	0.00	0.00
K	0.00	0.00	0.00	0.00	0.00	0.00	0.00	0.00	0.00	0.00	0.00	0.00	0.00	0.00	0.00	0.00	0.00	0.00	0.00	0.00	0.00	0.00	0.00	0.00
Sum	**8.00**	**8.00**	**8.00**	**8.00**	**8.00**	**8.00**	**8.00**	**8.00**	**8.00**	**8.00**	**8.00**	**8.00**	**8.00**	**8.00**	**8.00**	**8.00**	**8.00**	**8.00**	**8.00**	**8.00**	**8.00**	**8.00**	**8.00**	**8.00**
XPyp	**0.10**	**0.12**	**0.47**	**0.49**	**0.35**	**0.41**	**0.26**	**0.42**	**0.36**	**0.25**	**0.27**	**0.24**	**0.25**	**0.20**	**0.19**	**0.20**	**0.31**	**0.27**	**0.23**	**0.21**	**0.09**	**0.08**	**0.12**	**0.08**
XAlm	**0.64**	**0.58**	**0.49**	**0.47**	**0.54**	**0.54**	**0.53**	**0.54**	**0.56**	**0.52**	**0.54**	**0.52**	**0.52**	**0.65**	**0.61**	**0.59**	**0.60**	**0.55**	**0.54**	**0.56**	**0.65**	**0.64**	**0.64**	**0.63**
XGrs	**0.15**	**0.19**	**0.04**	**0.03**	**0.11**	**0.05**	**0.21**	**0.04**	**0.08**	**0.23**	**0.19**	**0.23**	**0.24**	**0.15**	**0.20**	**0.22**	**0.09**	**0.18**	**0.23**	**0.23**	**0.03**	**0.03**	**0.04**	**0.03**
XSps	**0.12**	**0.11**	/	/	/	/	/	/	/	/	/	/	/	/	/	/	/	/	/	/	**0.23**	**0.25**	**0.20**	**0.26**

O-Rim = outermost rim.

Table 4
Representative EPMA analyses of orthopyroxene and pigeonite.

Ideal cations	4.00	4.00	4.00	4.00	4.00	4.00	4.00	4.00	4.00	4.00	4.00	4.00	4.00	4.00	4.00	4.00	4.00	4.00	4.00	4.00	4.00	4.00	4.00	4.00
Ideal oxygens	6	6	6	6	6	6	6	6	6	6	6	6	6	6	6	6	6	6	6	6	6	6	6	6
Sample	HS83	HS83	HS84	HS84	HS86	HS86	HS88	HS88	HS88	HS88	HS88	HS88	HS88	HS88	HS88	HS90	HS90	HS90	HS92	HS92	HS92	HS92	HS92	HS92
	Opx14	Opx26	Opx5	Opx22	Opx5	Opx8	Opx12	Opx16	Opx21	Opx28	Opx29	Pgt33	Opx36	Opx37	Opx8	Opx5	Opx11	Opx21	Opx	Opx7	Opx12	Opx13	Opx14	Opx24
	/	/	/	/	/	/	/	/	/	/	/	/	Core	Rim	/	Rim	/	/	/	/	/	/	/	/
	Opx II	Opx III	Opx II	Opx II	Opx II	Opx II	Opx II	Opx II	Opx II	Opx I	Opx I	Opx II	Opx II	Opx II	Opx II	Opx II	Opx II	Opx II	Opx II	Opx II	Opx III	Opx III	Opx III	Opx II
wt %																								
SiO2	52.88	52.86	51.66	51.96	50.35	50.12	51.95	51.88	51.69	49.46	49.50	51.62	51.24	51.34	52.44	51.62	51.28	51.52	52.17	51.90	51.71	52.10	51.66	51.39
TiO2	0.15	0.02	0.11	0.02	0.06	0.31	0.00	0.09	0.00	0.01	0.01	0.14	0.05	0.00	0.07	0.05	0.09	0.12	0.09	0.08	0.00	0.00	0.17	0.10
Al2O3	1.88	1.46	1.33	1.32	1.23	1.26	0.49	0.52	0.90	0.78	1.01	0.28	0.51	0.39	0.76	1.57	2.45	2.30	1.61	1.53	1.70	1.52	1.52	1.54
Cr2O3	0.00	0.02	0.00	0.00	0.02	0.03	0.00	0.00	0.00	0.00	0.00	0.00	0.00	0.00	0.00	0.00	0.00	0.00	0.13	0.04	0.00	0.00	0.04	0.00
BaO	0.00	0.00	0.00	0.00	0.12	0.18	0.00	0.00	0.00	0.00	0.00	0.00	0.00	0.00	0.00	0.00	0.00	0.00	0.00	0.00	0.00	0.00	0.00	0.00
FeO	21.27	20.86	22.75	22.08	25.65	26.26	25.71	25.85	27.15	32.78	32.29	25.35	27.11	26.77	25.42	23.03	22.84	23.37	22.64	22.49	23.28	23.23	23.12	23.62
MnO	0.74	0.69	0.68	0.32	1.19	1.06	0.33	0.35	0.36	0.83	0.84	0.30	0.39	0.43	0.20	0.24	0.37	0.40	0.75	0.87	0.83	0.86	0.87	0.68
MgO	22.66	23.21	22.27	22.55	19.51	20.09	20.09	19.19	18.52	13.85	14.03	18.50	18.96	18.93	19.44	22.29	22.42	22.42	22.83	22.53	22.09	22.16	21.80	22.26
CaO	0.51	0.33	0.33	0.36	0.92	0.41	0.32	0.97	0.52	0.52	0.49	2.52	0.34	0.42	1.36	0.36	0.39	0.28	0.29	0.31	0.41	0.31	0.47	0.50
Na2O	0.04	0.04	0.00	0.04	0.00	0.00	0.00	0.00	0.00	0.00	0.00	0.00	0.00	0.00	0.00	0.00	0.00	0.04	0.03	0.03	0.04	0.03	0.04	0.04
K2O	0.02	0.01	0.00	0.02	0.00	0.01	0.00	0.00	0.00	0.00	0.00	0.00	0.03	0.00	0.00	0.00	0.07	0.00	0.00	0.02	0.04	0.00	0.04	0.04
ZrO2	0.00	0.00	0.00	0.00	0.00	0.00	0.06	0.03	0.04	0.01	0.00	0.01	0.05	0.01	0.01	0.00	0.00	0.00	0.00	0.00	0.00	0.00	0.00	0.00
Total	**100.15**	**99.50**	**99.13**	**98.67**	**99.05**	**99.73**	**98.95**	**98.88**	**99.18**	**98.24**	**98.17**	**98.72**	**98.68**	**98.29**	**99.70**	**99.16**	**99.91**	**100.45**	**100.54**	**99.80**	**100.10**	**100.21**	**99.69**	**100.17**
Ferric form	**HS83**	**HS83**	**HS84**	**HS84**	**HS86**	**HS86**	**HS88**	**HS88**	**HS88**	**HS88**	**HS88**	**HS88**	**HS88**	**HS88**	**HS88**	**HS90**	**HS90**	**HS90**	**HS92**	**HS92**	**HS92**	**HS92**	**HS92**	**HS92**
Si	1.96	1.96	1.94	1.95	1.93	1.91	1.99	1.99	1.99	1.98	1.98	1.99	1.98	1.99	1.99	1.94	1.91	1.91	1.93	1.93	1.93	1.94	1.94	1.91
Al	0.08	0.06	0.06	0.06	0.06	0.06	0.02	0.02	0.04	0.04	0.05	0.01	0.02	0.02	0.03	0.07	0.11	0.10	0.07	0.07	0.07	0.07	0.07	0.07
Ti	0.00	0.00	0.00	0.00	0.00	0.01	0.00	0.00	0.00	0.00	0.00	0.00	0.00	0.00	0.00	0.00	0.00	0.00	0.00	0.00	0.00	0.00	0.00	0.00
Cr	0.00	0.00	0.00	0.00	0.00	0.00	0.00	0.00	0.00	0.00	0.00	0.00	0.00	0.00	0.00	0.00	0.00	0.00	0.00	0.00	0.00	0.00	0.00	0.00
Ba	0.00	0.00	0.00	0.00	0.00	0.00	0.00	0.00	0.00	0.00	0.00	0.00	0.00	0.00	0.00	0.00	0.00	0.00	0.00	0.00	0.00	0.00	0.00	0.00
Fe3	0.00	0.01	0.05	0.04	0.08	0.11	0.00	0.00	0.00	0.00	0.00	0.00	0.02	0.00	0.00	0.05	0.08	0.08	0.07	0.06	0.08	0.06	0.05	0.11
Mg	1.25	1.29	1.25	1.26	1.11	1.14	1.14	1.10	1.06	0.83	0.84	1.06	1.09	1.09	1.10	1.25	1.24	1.24	1.26	1.25	1.23	1.23	1.22	1.24
Fe	0.66	0.64	0.66	0.66	0.74	0.72	0.82	0.83	0.87	1.10	1.08	0.82	0.86	0.86	0.81	0.67	0.63	0.64	0.63	0.64	0.65	0.67	0.67	0.63
Mn	0.02	0.02	0.02	0.01	0.04	0.03	0.01	0.01	0.01	0.03	0.03	0.01	0.01	0.01	0.01	0.01	0.01	0.01	0.02	0.03	0.03	0.03	0.03	0.02
Ca	0.02	0.01	0.01	0.01	0.04	0.02	0.01	0.04	0.02	0.02	0.02	0.10	0.01	0.02	0.06	0.01	0.02	0.01	0.01	0.01	0.02	0.01	0.02	0.02
Na	0.00	0.00	0.00	0.00	0.00	0.00	0.00	0.00	0.00	0.00	0.00	0.00	0.00	0.00	0.00	0.00	0.00	0.00	0.00	0.00	0.00	0.00	0.00	0.00
K	0.00	0.00	0.00	0.00	0.00	0.00	0.00	0.00	0.00	0.00	0.00	0.00	0.00	0.00	0.00	0.00	0.00	0.00	0.00	0.00	0.00	0.00	0.00	0.00
Zr	0.00	0.00	0.00	0.00	0.00	0.00	0.00	0.00	0.00	0.00	0.00	0.00	0.00	0.00	0.00	0.00	0.00	0.00	0.00	0.00	0.00	0.00	0.00	0.00
Sum	4.00	4.00	4.00	4.00	4.00	4.00	4.00	4.00	4.00	4.00	4.00	4.00	4.00	4.00	4.00	4.00	4.00	4.00	4.00	4.00	4.00	4.00	4.00	4.00
XMG	**0.64**	**0.65**	**0.62**	**0.64**	**0.55**	**0.56**	**0.58**	**0.55**	**0.54**	**0.42**	**0.43**	**0.53**	**0.55**	**0.55**	**0.56**	**0.63**	**0.63**	**0.62**	**0.63**	**0.63**	**0.62**	**0.62**	**0.61**	**0.61**

Table 5
Representative EPMA analyses of clinopyroxene.

Ideal cations	4.00	4.00	4.00	4.00	4.00	4.00	4.00	4.00	4.00	4.00	4.00	4.00	4.00	4.00	4.00	4.00	4.00
Ideal oxygens	6	6	6	6	6	6	6	6	6	6	6	6	6	6	6	6	6
Sample	HS83	HS83	HS83	HS83	HS83	HS86	HS86	HS88	HS88	HS88	HS88	HS88	HS88	HS90	HS90	HS92	HS92
	cpx12	cpx13	cpx17	cpx18	cpx29	cpx9	cpx14	cpx10	cpx13	cpx17	cpx25	cpx31	cpx38	cpx12	cpx19	cpx1	cpxi21
	rim	core	core	rim	/	core	/	rim	/	/	/	/	/	/	/	/	incl.
wt %																	
SiO2	50.89	50.08	50.23	51.14	49.41	49.04	50.94	53.28	53.17	53.59	52.65	53.00	51.80	52.72	51.82	50.20	52.19
TiO2	0.36	0.46	0.41	0.30	0.38	0.22	0.38	0.15	0.03	0.07	0.14	0.09	0.09	0.05	0.06	0.45	0.16
Al2O3	3.64	5.28	4.36	3.59	4.81	2.66	1.97	1.04	1.27	1.30	0.99	0.99	0.79	0.74	0.98	3.40	1.23
Cr2O3	0.00	0.00	0.00	0.00	0.00	0.06	0.06	0.00	0.00	0.00	0.00	0.00	0.00	0.00	0.00	0.08	0.00
BaO	0.00	0.00	0.00	0.00	0.00	0.06	0.01	0.00	0.00	0.00	0.00	0.00	0.00	0.00	0.00	0.00	0.00
FeO	8.03	9.45	8.24	8.02	9.59	9.81	8.57	8.57	8.27	8.41	8.97	9.80	9.18	7.45	7.48	8.14	7.80
MnO	0.37	0.52	0.30	0.23	0.34	0.50	0.34	0.10	0.08	0.05	0.09	0.11	0.07	0.18	0.16	0.36	0.20
MgO	13.41	12.65	12.98	13.54	12.84	13.36	13.62	14.00	13.99	14.05	13.40	12.22	13.33	15.14	14.81	13.61	14.61
CaO	22.49	21.93	22.22	22.63	21.43	21.88	22.71	22.14	21.57	22.01	21.63	21.32	21.73	21.35	21.71	21.18	21.60
Na2O	0.62	0.63	0.68	0.69	0.59	0.53	0.43	0.00	0.00	0.00	0.00	0.00	0.00	0.43	0.44	0.63	0.53
K2O	0.45	0.55	0.65	0.00	0.80	0.01	0.00	0.00	0.00	0.00	0.01	0.04	0.00	0.00	0.00	0.00	0.00
ZrO2	0.00	0.00	0.00	0.00	0.00	0.00	0.00	0.44	0.65	0.71	0.47	0.53	0.54	0.00	0.00	0.00	0.00
Total	**97.69**	**97.84**	**96.44**	**95.19**	**96.32**	**98.13**	**99.03**	**99.72**	**99.03**	**100.19**	**98.35**	**98.10**	**97.53**	**98.06**	**97.46**	**98.05**	**98.32**
Ferric form	**HS83**	**HS83**	**HS83**	**HS83**	**HS83**	**HS86**	**HS86**	**HS88**	**HS88**	**HS88**	**HS88**	**HS88**	**HS88**	**HS90**	**HS90**	**HS92**	**HS92**
Si	1.88	1.83	1.86	1.89	1.83	1.86	1.91	2.00	2.00	2.00	2.00	2.00	1.99	1.98	1.96	1.90	1.96
Al	0.16	0.23	0.19	0.16	0.21	0.12	0.09	0.05	0.06	0.06	0.04	0.04	0.04	0.03	0.04	0.15	0.05
Ti	0.01	0.01	0.01	0.01	0.01	0.01	0.01	0.00	0.00	0.00	0.00	0.00	0.00	0.00	0.00	0.01	0.00
Cr	0.00	0.00	0.00	0.00	0.00	0.00	0.00	0.00	0.00	0.00	0.00	0.00	0.00	0.00	0.00	0.00	0.00
Ba	0.00	0.00	0.00	0.00	0.00	0.00	0.00	0.00	0.00	0.00	0.00	0.00	0.00	0.00	0.00	0.00	0.00
Fe3	0.13	0.15	0.15	0.10	0.19	0.19	0.10	0.00	0.01	0.00	0.01	0.04	0.00	0.03	0.06	0.08	0.05
Mg	0.74	0.69	0.72	0.75	0.71	0.76	0.76	0.78	0.79	0.78	0.76	0.70	0.76	0.85	0.84	0.77	0.82
Fe	0.12	0.14	0.10	0.15	0.11	0.13	0.17	0.27	0.26	0.26	0.29	0.32	0.30	0.21	0.18	0.18	0.19
Mn	0.01	0.02	0.01	0.01	0.01	0.02	0.01	0.00	0.00	0.00	0.00	0.00	0.00	0.01	0.01	0.01	0.01
Ca	0.89	0.86	0.88	0.90	0.85	0.89	0.91	0.89	0.87	0.88	0.88	0.88	0.90	0.86	0.88	0.86	0.87
Na	0.04	0.04	0.05	0.05	0.04	0.04	0.03	0.00	0.00	0.00	0.00	0.00	0.00	0.03	0.03	0.05	0.04
K	0.02	0.03	0.03	0.00	0.04	0.00	0.00	0.00	0.00	0.00	0.00	0.00	0.00	0.00	0.00	0.00	0.00
Zr	0.00	0.00	0.00	0.00	0.00	0.00	0.00	0.01	0.01	0.01	0.01	0.01	0.01	0.00	0.00	0.00	0.00
Sum	**4.00**	**4.00**	**4.00**	**4.00**	**4.00**	**4.00**	**4.00**	**4.00**	**4.00**	**4.00**	**4.00**	**4.00**	**4.00**	**4.00**	**4.00**	**4.00**	**4.00**
XMg	**0.74**	**0.69**	**0.73**	**0.75**	**0.70**	**0.70**	**0.73**	**0.74**	**0.74**	**0.75**	**0.72**	**0.66**	**0.72**	**0.78**	**0.78**	**0.74**	**0.76**

incl. = Inclusion.

rocks and their internal relationships. These are granitic gneisses, granulites, hornblende-biotite gneisses and widespread migmatitic gneisses that occur as massive bodies. Locally, these rocks are interlayered with amphibolites and aluminous amphibolite-facies metapelites. Thus, the precursors of these high-grade rocks were predominantly of granitoid and/or volcano-sedimentary origin with a predominance of igneous rocks over sedimentary assemblages. Undeformed post-kinematic granites and syenites intruded into these high-grade rocks. Pegmatites with well-developed large muscovite books are associated with these post-orogenic granites.

Pyroxene granulites with well-developed melanocratic and leucocratic layers and massive charnockites occur as small, solitary outcrops in inselbergs. The granulites and charnockitic rocks look similar to those found elsewhere in the MB of Tanzania (Figs. 1A,B; Table 1). Foliations in the high-grade Songea rocks principally strike N–S to NNE–SSW with shallow dips and a down-dip stretching lineation of ~100/10. Small-scale isoclinal, recumbent folds with E–W trending axes are developed in some of these rocks. High-angle shear zones are frequent and converted the granitoids into mylonites and schists.

Schenk et al. (2004) reported a monazite U–Pb age of 1950 ± 30 Ma for a UHT metapelitic assemblage from the region between Songea and Mbamba Bay at Lake Malawi. These rocks belong to a Palaeoproterozoic segment of the crust known as Ubendian belt and are separated from the Pan-African assemblage discussed below by a major shear zone that defines the margin of the Mozambique belt in southwestern Tanzania.

3. Petrography and mineral chemistry

Rocks in the Songea area are only exposed along steep slopes, in inselbergs or in quarries. Four main lithological units are recognized: (1) metapelitic rocks, (2) migmatic gneisses, (3) charnockitic and enderbitic gneisses, and (4) nearly undeformed granitic rocks. Exposed rocks are usually fresh with only minor retrograde mineral phases. The mineral assemblages of selected samples of all four lithological units are summarized in Table 2, and chemical compositions of selected minerals are given in Tables 3–6 and Supplement Tables 2–5. The microprobe analytical procedure is summarized in the Appendix. Mineral abbreviations are after Bucher and Grapes (2011).

3.1. Metapelite

Amphibolite-facies metapelites are rare and found mainly in the north and south of the study area (Fig. 1B). Those in the north, near the town of Songea (Fig. 1B), are fine-grained, dark gray, foliated rocks showing recrystallized fabrics in thin section with poikilitic garnet (Grt III), biotite and hornblende (Fig. 2A). The mineral assemblage in samples HS 74-76 (Fig. 1B) consists of garnet (Grt) – biotite (Bt) – plagioclase (Pl) - K-feldspar (Kfs) – quartz (Qtz) – amphibole (Am) – ilmenite (Ilm) – clinozoisite/epidote (Czo/Ep) – dolomite (Dol) – calcite (Cal) (Table 2). Garnet (Grt III) is 0.5 to 1.5 mm in size and nearly homogeneous in composition (X_{Alm} = 0.64–0.58, X_{Prp} = 0.10–0.12, X_{Grs} = 0.15–0.19, and X_{Sps} = 0.12–0.11) with only a slight decrease, from core to rim, in

Table 6
Representative EPMA analyses of plagioclase.

Ideal cations	5.00	5.00	5.00	5.00	5.00	5.00	5.00	5.00	5.00	5.00	5.00	5.00	5.00	5.00	5.00	5.00	5.00	5.00	5.00	5.00	5.00	5.00	5.00	5.00
Ideal oxygens	8	8	8	8	8	8	8	8	8	8	8	8	8	8	8	8	8	8	8	8	8	8	8	8
Sample	HS75	HS75	HS75	HS75	HS81	HS81b	HS81b	HS81b	HS82	HS82	HS82	HS82	HS83	HS83	HS84	HS84	HS84	HS84	HS84	HS84	HS88	HS88	HS88	HS90
	Pl8	Pl1	Pl7a	Pl18	Pl7	Pl4	Pl7	Pl15	Pl20	plag22i	plag21i	Pl3	Pl10	Pl21	Pl4	Pl9	Pl24	Pl37	Pl31	Pl23	Pl32	Pl35	Pl40	Pl8
	/	/	/	/	/	/	/	/	Incl.	Incl.	Incl.	/	/	Core	/	/	/	/	/	Rim	/	/	/	Core
wt %																								
SiO2	61.78	58.94	59.34	60.76	60.45	55.07	57.80	58.66	52.55	58.63	56.86	59.74	54.65	55.91	54.56	57.02	52.60	57.25	52.81	54.26	56.99	56.01	56.90	55.94
TiO2	0.00	0.09	0.00	0.10	0.01	0.01	0.05	0.02	0.04	0.00	0.05	0.00	0.04	0.04	0.07	0.00	0.00	0.01	0.00	0.01	0.04	0.04	0.03	0.02
Al2O3	23.27	25.58	24.72	24.40	24.32	27.91	26.19	25.66	29.42	25.20	25.92	24.73	28.53	27.46	27.49	26.69	29.23	26.11	29.48	27.87	27.55	28.25	27.37	27.53
Cr2O3	0.00	0.00	0.00	0.00	0.00	0.00	0.00	0.00	0.00	0.00	0.00	0.00	0.00	0.00	0.00	0.00	0.00	0.00	0.00	0.00	0.00	0.00	0.00	0.00
BaO	0.00	0.00	0.00	0.00	0.00	0.00	0.00	0.00	0.00	0.00	0.00	0.00	0.00	0.00	0.00	0.00	0.00	0.00	0.00	0.00	0.00	0.00	0.00	0.00
FeO	0.00	0.00	0.00	0.00	0.00	0.00	0.00	0.00	0.00	0.00	0.00	0.00	0.00	0.00	0.00	0.00	0.00	0.00	0.00	0.00	0.00	0.00	0.00	0.00
MnO	0.16	0.12	0.10	0.17	0.00	0.00	0.00	0.00	0.05	0.05	0.00	0.06	0.09	0.06	0.00	0.00	0.00	0.04	0.00	0.04	0.00	0.00	0.02	0.00
MgO	0.00	0.00	0.00	0.05	0.03	0.00	0.00	0.00	0.19	0.15	0.17	0.00	0.02	0.00	0.60	0.00	0.01	0.01	0.01	0.00	0.00	0.00	0.00	0.15
CaO	4.61	7.25	6.71	5.81	5.74	10.46	8.35	7.59	11.95	7.24	8.33	6.71	11.01	9.75	9.16	9.03	11.81	8.24	12.24	10.45	9.69	10.02	10.02	9.65
Na2O	8.89	7.27	7.57	8.16	8.35	5.65	6.74	7.25	4.83	7.28	6.55	7.29	5.23	5.79	5.34	6.26	4.73	6.73	4.53	5.54	6.20	5.68	6.15	5.94
K2O	0.03	0.04	0.06	0.03	0.20	0.12	0.12	0.17	0.13	0.13	0.21	0.41	0.25	0.29	0.24	0.36	0.16	0.33	0.20	0.22	0.19	0.15	0.15	0.17
Total	**98.74**	**99.29**	**98.50**	**99.48**	**99.10**	**99.22**	**99.25**	**99.35**	**99.16**	**98.68**	**98.09**	**98.94**	**99.82**	**99.30**	**97.46**	**99.36**	**98.54**	**98.72**	**99.27**	**98.39**	**100.66**	**100.15**	**100.64**	**99.40**
Ferrous form	**HS75**	**HS75**	**HS75**	**HS75**	**HS81**	**HS81b**	**HS81b**	**HS81b**	**HS82**	**HS82**	**HS82**	**HS82**	**HS83**	**HS83**	**HS84**	**HS84**	**HS84**	**HS84**	**HS84**	**HS84**	**HS88**	**HS88**	**HS88**	**HS90**
Si	2.77	2.65	2.68	2.71	2.71	2.50	2.60	2.64	2.40	2.65	2.60	2.69	2.47	2.53	2.51	2.57	2.42	2.60	2.41	2.49	2.54	2.51	2.54	2.53
Al	1.23	1.35	1.32	1.28	1.29	1.49	1.39	1.36	1.58	1.34	1.39	1.31	1.52	1.47	1.49	1.42	1.58	1.40	1.58	1.51	1.45	1.49	1.44	1.47
Ti	0.00	0.00	0.00	0.00	0.00	0.00	0.00	0.00	0.00	0.00	0.00	0.00	0.00	0.00	0.00	0.00	0.00	0.00	0.00	0.00	0.00	0.00	0.00	0.00
Cr	0.00	0.00	0.00	0.00	0.00	0.00	0.00	0.00	0.00	0.00	0.00	0.00	0.00	0.00	0.00	0.00	0.00	0.00	0.00	0.00	0.00	0.00	0.00	0.00
Ba	0.00	0.00	0.00	0.00	0.00	0.00	0.00	0.00	0.00	0.00	0.00	0.00	0.00	0.00	0.00	0.00	0.00	0.00	0.00	0.00	0.00	0.00	0.00	0.00
Mg	0.00	0.00	0.00	0.00	0.00	0.00	0.00	0.00	0.01	0.01	0.01	0.00	0.00	0.00	0.04	0.00	0.00	0.00	0.00	0.00	0.00	0.00	0.00	0.01
Fe	0.00	0.00	0.00	0.00	0.00	0.00	0.00	0.00	0.00	0.00	0.00	0.00	0.00	0.00	0.00	0.00	0.00	0.00	0.00	0.00	0.00	0.00	0.00	0.00
Mn	0.01	0.00	0.00	0.01	0.00	0.00	0.00	0.00	0.00	0.00	0.00	0.00	0.00	0.00	0.00	0.00	0.00	0.00	0.00	0.00	0.00	0.00	0.00	0.00
Ca	0.22	0.35	0.32	0.28	0.28	0.51	0.40	0.37	0.59	0.35	0.41	0.32	0.53	0.47	0.45	0.44	0.58	0.40	0.60	0.51	0.46	0.48	0.48	0.47
Na	0.77	0.63	0.66	0.71	0.73	0.50	0.59	0.63	0.43	0.64	0.58	0.64	0.46	0.51	0.48	0.55	0.42	0.59	0.40	0.49	0.54	0.49	0.53	0.52
K	0.00	0.00	0.00	0.00	0.01	0.01	0.01	0.01	0.01	0.01	0.01	0.02	0.01	0.02	0.01	0.02	0.01	0.02	0.01	0.01	0.01	0.01	0.01	0.01
Sum	**5.00**	**4.99**	**4.99**	**5.00**	**5.01**	**5.01**	**5.00**	**5.00**	**5.02**	**5.00**	**5.00**	**4.99**	**5.00**	**5.00**	**4.99**	**5.00**	**5.01**	**5.01**	**5.00**	**5.01**	**5.00**	**4.99**	**5.01**	**5.00**
XAn	**0.22**	**0.35**	**0.33**	**0.28**	**0.27**	**0.50**	**0.40**	**0.36**	**0.57**	**0.35**	**0.41**	**0.33**	**0.53**	**0.47**	**0.48**	**0.43**	**0.57**	**0.40**	**0.59**	**0.50**	**0.46**	**0.49**	**0.47**	**0.47**

Incl. = Inclusion.

Fe and an increase in Ca and Mg (Table 3). Biotite varies in X_{Mg} between 0.51 and 0.55 and forms 1–4 mm long poikilitic flakes with minor concentrations in TiO_2 (up to 2.27 wt. %), (Supplement Table 2). Amphibole is locally intergrown with biotite (Fig. 2A) and is classified as tschermakite (Leake et al., 1997) (Supplement Table 3). Plagioclase is sodium-rich with an albite component ranging between 0.64 and 0.78 (Table 6). Textural observations and chemical compositions of the described minerals above indicate, that these metapelites have been formed at medium pressure and temperature under amphibolite facies conditions.

Metapelite samples collected in the south of the study area (HS 100–103) exhibit a different mineral assemblage consisting of biotite (Bt) – plagioclase (Pl) – quartz (Qtz) – sillimanite (Sil) – ilmenite (Ilm) ± garnet (Grt) ± K-feldspar (Kfs) ± muscovite (Ms) (Fig. 2B). These rocks are well foliated due to abundant sillimanite and biotite. Garnet is 0.5–1.5 mm in size and is typically zoned, consistent with

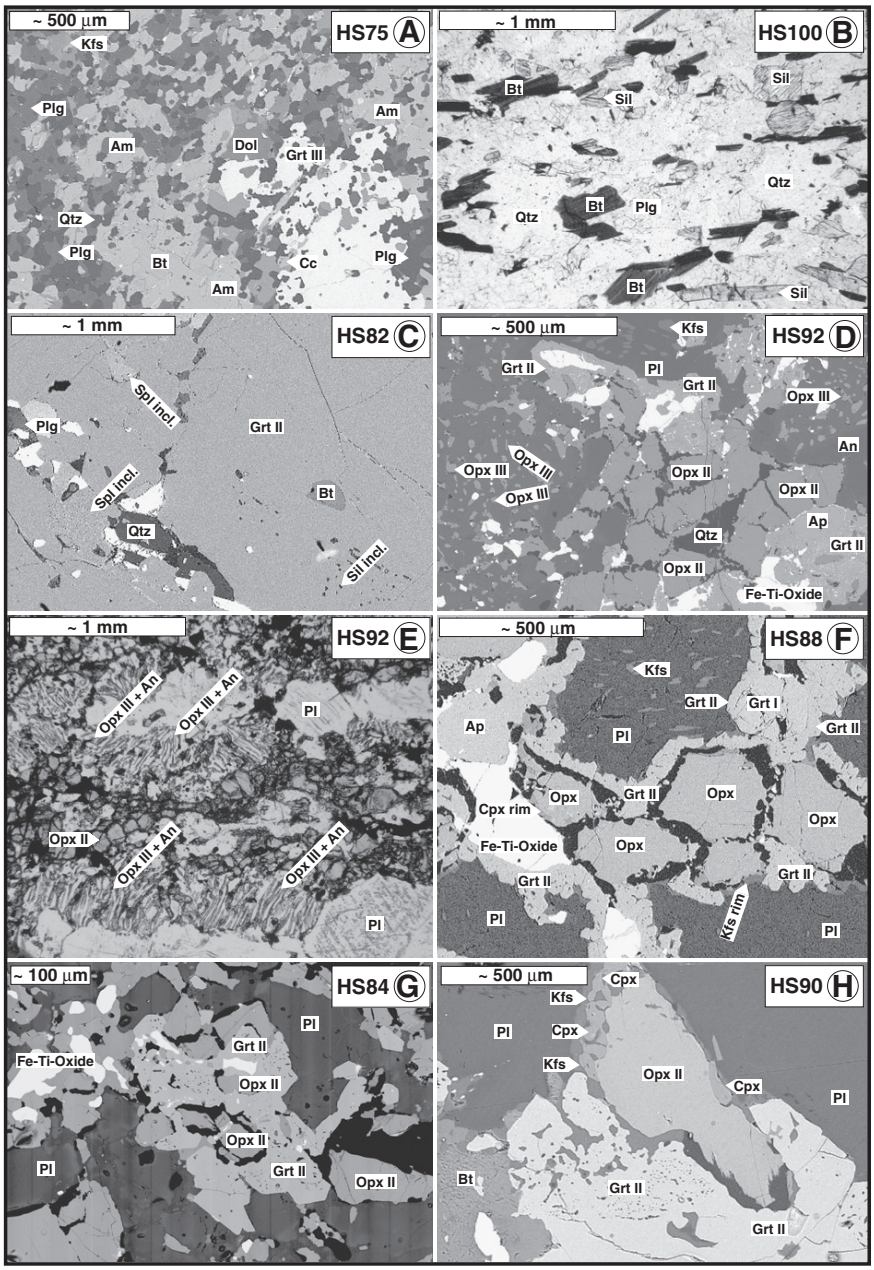

Fig. 2. (A) Back-scattered electron (BSE) image of a Grt–Bt–Am–Pl–Qtz–Dol–Cc metapelite from the northern part of the working area (HS75). Grt, Bt, and Am show poikilitic textures. (B) Photomicrograph of a Grt–Sil–Bt–Pl–Qtz metapelite (HS100) from the southern part of the study area. Sillimanite forms coarse-grained prismatic crystals within an equigranular matrix of quartz (Qtz) and plagioclase (Pl). (C) BSE image of garnet with inclusions of spinel (Spl), sillimanite (Sil), biotite (Bt), plagioclase (Pl), quartz (Qtz), and Fe–Ti-oxides in sample HS82. (D) BSE image of granulite-facies charnockitic mineral assemblage Opx (II and III) – Grt II – Fe–Ti-oxides – Cpx – Pl – Qtz (HS92). Two generations of Opx can be seen: (1) large, rounded grains (Opx II) and (2) pseudomorphs of small "worm-like" Opx crystals intergrown with An-rich plagioclase after Grt (Opx III). New Grt II coronas grows around Fe–Ti-oxides. (E) Photomicrograph of the same sample as shown in Fig. 2d. Matrix Opx II and large pseudomorphs of Opx III and An-rich Pl after Grt are seen. Pl shows antiperthitic textures. (F) BSE image of sample HS88. Grt II growth around Grt I. Orthopyroxene exhibits a small rim of Cpx, followed by coronas of Qtz and Grt II. A second type of Grt II coronas is developed around Fe–Ti-oxides. (G) BSE image of sample HS84. Grt II coronas are seen around Opx and Fe–Ti-oxides. (H) BSE image showing reaction texture between Opx + Pl + Kfs + H_2O forming Grt + Bt + Cpx + Qtz (sample HS90).

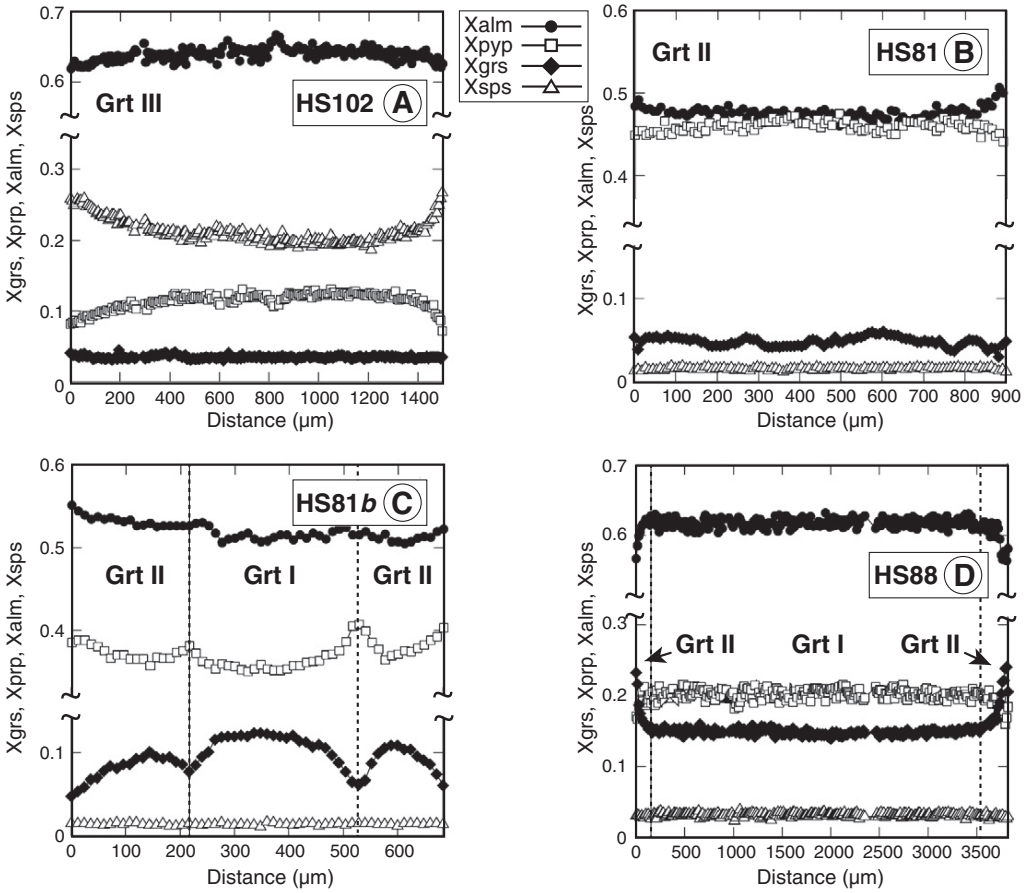

Fig. 3. Representative microprobe traverses: (A) Retrograde zonation of garnet in metapelitic sample HS102. (B) Homogeneous zonation of garnet (Grt II) from garnet-rich granitoid orthogneiss sample HS81. (C) Garnet zonation in a granitoid orthogneiss. The zonation in Ca indicates a second growth phase. The distinct zonation first shows the formation of Grt I and second the growth of Grt II in sample HS81*b*. (D) Zonation in a large "relic" garnet of charnockitic mineral assemblage in sample HS88. Most garnets are homogeneous in chemical composition, only the outermost rims record a change from Grt I to Grt II. Texturally, the outermost rims belong to the same garnet type as found as coronas around Opx and Fe–Ti-oxides (Figs. 3d, f, g). An increase in grossular and a decrease in almandine content are evident in the newly grown rims.

retrograde overprinting. X_{Sps} is increasing from core towards the rim and varies between 0.20 (core) and 0.26 (rim), X_{Alm} (0.66 core – 0.62 rim) and X_{Pyp} (0.12 core–0.06 rim) are decreasing from the core towards to the rim, and X_{Grs} ratio is about 0.04 and thus almost constant (Table 3, Fig. 3A). Due to the mineral chemistry, we also classified the garnets from these metapelitic samples as late-formed Grt III. Sillimanite occurs as idiomorphic, large prismatic grains. Biotite forms 0.5–1 mm grains, is homogenous in mineral chemical composition with an X_{Mg} ratio of about 0.65; the TiO_2-content is up to 3.4 wt. % and the F-content is 0.14–0.23 wt. % (Supplementary Table 2). Plagioclase in the matrix varies in X_{Ab} between 0.71–0.73 (Table 7), whereas plagioclase inclusions in garnet are rich in sodium and show an X_{Ab} of 0.86 (Table 7). Chemical compositions of the investigated minerals show that these metapelites were formed at medium pressure and temperature under amphibolite-facies conditions in the sillimanite stability field.

3.2. Migmatitic gneiss

Migmatitic gneisses are generally fresh and were sampled in several quarries. Samples HS81–HS82 were collected in a forest about 10 km to the west of Songea town, sample HS87 was taken from Lipokela Quarry along the main road west of Songea, samples HS93–HS96 where collected in the large Mpitimbi Quarry about 15 km south of Songea, and sample HS99 was taken in the south of the study area (Fig. 1B). The observed mineral assemblage in thin section is K-feldspar (Kfs) – plagioclase (Pl) – quartz (Qtz) – biotite (Bt) ± garnet (Grt) ± amphibole (Am) ± ilmenite/Ti-hematite (Ilm/Ti-Hem) ± rutile (Rt) ± clinozoisite/epidote/allanite (Cz/Ep/Aln) ± muscovite (Ms) ± sillimanite (Sil) (Table 2). Some enclaves (HS81, HS81b, HS82) with large 10–30 mm garnets were found within the migmatic rocks, and the mineral assemblage comprises garnet (Grt) — biotite (Bt) — plagioclase (Pl) — K—feldspar (Kfs) — ilmenite (Ilm).

Garnet in sample HS81 can be subdivided into two generations due to their chemical composition from core to rim (Grt I and Grt II). Both generations show high pyrope and almandine ratios, and the first generation (Grt I) is characterized by an increase in X_{Pyp} from core (0.47) to the rim (0.49) and a decrease in X_{Alm} from core (0.49) to the rim (0.47) (Table 3). The opposite zonation is seen in the second generation (Grt II) of sample HS81. X_{Pyp} decreases from core (0.48) to rim (0.44) and X_{Alm} increases from core (0.46) to rim (0.51) (Fig. 3B). X_{Grs} varies between 0.03 and 0.05 in both generations (Fig. 3B; Table 3). In contrast, garnets in sample HS81*b* show a distinct zonation and represent both generations (Grt I and Grt II) in one profile (Fig. 3C). X_{Grs} first decreases from core (0.13) to rim (0.05), then increases (0.11), and finally decreases again towards the outermost rim (0.05) (Fig. 3C). X_{Pyp} shows the opposite pattern in first increasing from core (0.35) to rim (0.42), then decreasing (0.37) and finally increasing again close to the garnet rim (0.41). Another, garnet (Grt II) from this particular sample shows an even higher X_{Grs} ratio of up to 0.21, a X_{Pyp} ratio of 0.26 and X_{Alm} of 0.53 (Table 3). The two garnet generations in sample HS81 and the distinct garnet zonation

Table 7
Representative EPMA analyses of plagioclase and K-feldspar.

Ideal cations	5.00	5.00	5.00	5.00	5.00	5.00	5.00	5.00	5.00	5.00	5.00	5.00	5.00	5.00	5.00	5.00	5.00	5.00	5.00	5.00	5.00
Ideal oxygens	8	8	8	8	8	8	8	8	8	8	8	8	8	8	8	8	8	8	8	8	8
Sample	**HS90**	**HS90**	**HS92**	**HS92**	**HS92**	**HS92**	**HS92**	**HS92**	**HS102**	**HS102**	**HS102**	**HS102**	**HS81**	**HS81b**	**HS81b**	**HS81b**	**HS86**	**HS88**	**HS88**	**HS90**	**HS90**
	Pl9	**Pl18**	**Pl23**	**Pl25**	**Pl6**	**Pl11**	**Pl**	**Pl15**	**Pl8**	**Pl9**	**Pl14**	**Pl24**	**Kfs8**	**Kfs6**	**Kfs21**	**Kfs23**	**Kfs13**	**Kfs30**	**Kfs39**	**Kfs10**	**Kfs17**
	Rim	/	/	/	/	/	/	/	/	/	**Incl.**	**Rim**	/	**Incl.**	/		/	/	/	**Core**	**Rim**
wt %																					
SiO2	56.94	56.24	53.61	56.69	46.88	48.58	55.16	55.35	61.04	60.65	60.70	61.50	64.35	63.99	62.64	64.34	62.52	61.92	64.29	64.58	64.44
TiO2	0.01	0.00	0.03	0.05	0.05	0.04	0.04	0.00	0.03	0.03	0.01	0.02	0.00	0.01	0.03	0.00	0.00	0.00	0.15	0.13	0.05
Al2O3	27.29	27.09	28.70	27.00	31.81	31.15	27.31	27.61	24.78	24.94	26.82	24.79	18.69	18.48	18.37	18.96	18.78	18.84	18.28	18.33	18.51
Cr2O3	0.00	0.00	0.02	0.01	0.01	0.01	0.00	0.01	0.00	0.00	0.00	0.00	0.00	0.00	0.00	0.00	0.11	0.00	0.00	0.00	0.00
BaO	0.00	0.00	0.44	0.34	0.21	0.15	0.11	0.13	0.00	0.00	0.00	0.00	0.00	0.29	0.29	0.40	1.50	0.26	0.00	0.00	0.00
FeO	0.00	0.00	0.00	0.00	0.00	0.00	0.00	0.00	0.00	0.00	0.00	0.00	0.00	0.00	0.00	0.00	0.00	0.00	0.00	0.00	0.00
MnO	0.11	0.07	0.07	0.00	0.00	0.00	0.00	0.01	0.00	0.00	0.00	0.00	0.00	0.03	0.02	0.00	0.04	0.00	0.00	0.05	0.08
MgO	0.00	0.00	0.16	0.27	0.32	0.00	0.02	0.19	0.00	0.00	0.00	0.00	0.00	0.02	0.00	0.00	0.00	0.00	0.00	0.20	0.04
CaO	9.75	9.50	11.19	9.18	15.66	14.83	9.91	10.00	5.83	6.24	2.66	5.92	0.07	0.13	0.08	0.06	0.05	0.24	0.00	0.00	0.03
Na2O	6.16	6.06	4.86	5.72	2.18	2.76	5.55	5.58	8.49	8.23	8.97	8.41	1.51	1.36	1.43	0.78	0.46	0.70	0.64	1.11	0.35
K2O	0.17	0.24	0.16	0.25	0.09	0.04	0.27	0.20	0.25	0.20	0.19	0.15	14.33	14.30	14.18	14.87	15.48	15.50	15.69	14.97	16.08
ZrO2	0.00	0.00	0.00	0.00	0.00	0.00	0.00	0.00	0.00	0.00	0.00	0.00	0.00	0.00	0.00	0.00	0.00	1.12	0.00	0.00	0.00
Total	**100.43**	**99.20**	**99.24**	**99.51**	**97.21**	**97.56**	**98.37**	**99.08**	**100.42**	**100.29**	**99.35**	**100.79**	**98.95**	**98.61**	**97.04**	**99.41**	**98.94**	**99.66**	**99.05**	**99.37**	**98.88**
Ferrous form	**HS90**	**HS90**	**HS92**	**HS92**	**HS92**	**HS92**	**HS92**	**HS92**	**HS102**	**HS102**	**HS102**	**HS102**	**HS81**	**HS81b**	**HS81b**	**HS81b**	**HS86**	**HS88**	**HS88**	**HS90**	**HS90**
Si	2.55	2.55	2.45	2.56	2.21	2.27	2.52	2.51	2.70	2.69	2.69	2.71	2.99	2.99	2.97	2.98	2.95	2.93	2.99	2.99	2.99
Al	1.44	1.45	1.54	1.44	1.77	1.72	1.47	1.48	1.29	1.30	1.40	1.29	1.02	1.02	1.03	1.04	1.05	1.05	1.00	1.00	1.01
Ti	0.00	0.00	0.00	0.00	0.00	0.00	0.00	0.00	0.00	0.00	0.00	0.00	0.00	0.00	0.00	0.00	0.00	0.00	0.01	0.00	0.00
Cr	0.00	0.00	0.00	0.00	0.00	0.00	0.00	0.00	0.00	0.00	0.00	0.00	0.00	0.00	0.00	0.00	0.00	0.00	0.00	0.00	0.00
Ba	0.00	0.00	0.01	0.01	0.00	0.00	0.00	0.00	0.00	0.00	0.00	0.00	0.00	0.01	0.01	0.01	0.03	0.00	0.00	0.00	0.00
Mg	0.00	0.00	0.01	0.02	0.02	0.00	0.00	0.01	0.00	0.00	0.00	0.00	0.00	0.00	0.00	0.00	0.00	0.00	0.00	0.01	0.00
Fe	0.00	0.00	0.00	0.00	0.00	0.00	0.00	0.00	0.00	0.00	0.00	0.00	0.00	0.00	0.00	0.00	0.00	0.00	0.00	0.00	0.00
Mn	0.00	0.00	0.00	0.00	0.00	0.00	0.00	0.00	0.00	0.00	0.00	0.00	0.00	0.00	0.00	0.00	0.00	0.00	0.00	0.00	0.00
Ca	0.47	0.46	0.55	0.44	0.79	0.74	0.49	0.49	0.28	0.30	0.13	0.28	0.00	0.01	0.00	0.00	0.00	0.01	0.00	0.00	0.00
Na	0.53	0.53	0.43	0.50	0.20	0.25	0.49	0.49	0.73	0.71	0.77	0.72	0.14	0.12	0.13	0.07	0.04	0.06	0.06	0.10	0.03
K	0.01	0.01	0.01	0.01	0.01	0.00	0.02	0.01	0.01	0.01	0.01	0.01	0.85	0.85	0.86	0.88	0.93	0.94	0.93	0.88	0.95
Zr	0.00	0.00	0.00	0.00	0.00	0.00	0.00	0.00	0.00	0.00	0.00	0.00	0.00	0.00	0.00	0.00	0.00	0.03	0.00	0.00	0.00
SO3	0.00	0.00	0.00	0.00	0.00	0.00	0.00	0.00	0.00	0.00	0.00	0.00	0.00	0.00	0.00	0.00	0.00	0.00	0.00	0.00	0.00
Cl	0.00	0.00	0.00	0.00	0.00	0.00	0.00	0.00	0.00	0.00	0.00	0.00	0.00	0.00	0.03	0.00	0.00	0.00	0.00	0.00	0.00
F	0.00	0.00	0.00	0.00	0.00	0.00	0.00	0.00	0.00	0.00	0.00	0.00	0.00	0.00	0.02	0.00	0.00	0.00	0.00	0.00	0.00
Sum	5.00	5.00	5.00	4.98	5.00	4.99	4.99	5.00	5.02	5.01	5.00	5.01	5.00	4.99	5.01	4.98	5.01	4.99	4.99	5.00	4.99
XAn	**0.47**	**0.46**	**0.56**	**0.46**	**0.79**	**0.75**	**0.49**	**0.49**	**0.27**	**0.29**	**0.14**	**0.28**	/	/	/	/	/	/	/	/	/
XKfs	/	/	/	/	/	/	/	/	/	/	/	/	**0.86**	**0.87**	**0.87**	**0.93**	**0.96**	**0.94**	**0.94**	**0.90**	**0.97**

in sample HS81b may reflect a two — phase growth, one prograde and one retrograde. Garnet (Grt II) of sample HS82 shows minor zonation effects. X_{Pyp} decreases from core (0.42) to rim (0.36), whereas X_{Alm} and X_{Grs} show the opposite zonation and increase from core (0.54) to rim (0.56) and (0.04) to (0.08), respectively (Table 3). The X_{Mg} (Mg/(Mg + Fe) value is 0.4 — 0.5 in all analyzed migmatitic gneiss samples (Table 3).

Garnets occasionally contain small inclusions of spinel and sillimanite (Fig. 2C) in addition to biotite, quartz, plagioclase, and ilmenite. Sillimanite inclusions occur as fine needles and former matrix sillimanite probably reacted away due to the formation of anorthite — rich plagioclase.

Plagioclase inclusions in garnet (Grt II) were analyzed in sample HS82. Plagioclase inclusions close to garnet cores show an X_{An} ratio of up to 0.57, decreasing to values of about 0.41 towards to the rim and further decreasing to 0.35 close to the garnet rims (Table 6). Matrix plagioclase in sample HS82 has nearly the same composition as plagioclase inclusions close to garnet rims (Table 6).

Matrix plagioclase of samples HS81 and HS81b exhibits exsolution of K—feldspar (antiperthite) and X_{An} in plagioclase varies between 0.27 and 0.5 (Table 6). K — feldspar shows exsolution lamellae of albite (perthite), and the X_{Kfs} varies between 0.86 and 0.93 (Table 7).

The chemical composition of biotite is characterized by an X_{Mg} ranging from 0.69 to 0.81 and high TiO_2 — and F-contents of 3.61–5.38 wt.% and 0.69–1.96 wt.%, respectively (Supplement Table 2). Muscovite only occurs as small flakes. Muscovite and clinozoisite/epidote/allanite represent retrograde minerals formed during upper greenschist– to lower amphibolite-facies conditions. Spinel inclusions are mainly found in garnet cores together with Fe-Ti-oxides and have an X_{Mg} ranging between 0.5 and 0.6 (Supplement Table 4). In summary, textural observations in thin section together with mineral chemical composition and zonation in garnets show that these migmatitic gneisses define a prograde metamorphic *P–T* path up to granulite-facies conditions and then became retrogressed to upper greenschist- to lower amphibolite-facies conditions.

3.3. Charnockitic gneiss

Charnockitic gneiss samples HS83 and 84 were sampled in a forest about 10 km west of Songea, from the Lipokela Quarry along the main road west of Songea (samples HS86; HS88-HS90), and close to Litetema, about 30 km to the west of Songea (samples HS91 and HS92). All samples are fresh, well foliated and consist of garnet (Grt) – orthopyroxene (Opx) – pigeonite (Pgt) – clinopyroxene (Cpx) – amphibole (Am) – biotite (Bt) – K-feldspar (Kfs) – plagioclase (Pl) – quartz (Qtz) – ilmenite/Ti-hematite (Ilm/Ti-Hem) ± scapolite (Scp). Selected mineral analyses are presented in Tables 3–7 and Supplement Tables 2–4.

Garnet usually occurs as 10 to 250 μm-wide rims around orthopyroxene or ilmenite/Ti-hematite (Figs. 2D, F, G, H). Pseudomorphs of anorthite-rich plagioclase and orthopyroxene (Opx III) after garnet indicate that the rocks originally contained individual garnet grains (Grt I). In fact, some large garnet relics were identified in two samples (HS88 and HS83) and are interpreted to have formed during prograde metamorphism. In sample HS88, a new garnet rim (Grt II) grew around the older core (Grt I; Fig. 2F), showing nearly the same chemical composition as the garnet coronas around orthopyroxene (Table 3). The X_{Pyp} of both garnet generations is similar, whereas X_{Grs} increases from 0.15 (Grt I) to 0.23 (Grt II) and X_{Alm} decreases from 0.63 (Grt I) to 0.57 (Grt II) at the outermost part of the measured profile through a large garnet grain with a newly grown rim (Fig. 3D; Table 3). Two different textural types with garnet coronas were observed: (a) garnet coronas around orthopyroxene (Figs. 2F, G) and (b) garnet coronas around Fe-Ti-oxides (Figs. 2D, F, G). Where garnet grows around orthopyroxene, a narrow rim of clinopyroxene and a quartz-corona around orthopyroxene is developed (Fig. 2F). In contrast, coronas around ilmenite/Ti-hematite do not show quartz and clinopyroxene rims; instead, garnets are usually full of small ilmenite/Ti-hematite/hematite and some clinopyroxene inclusions.

Orthopyroxene is abundant in most samples and usually forms subidiomorphic grains, 0.1-3 mm in size, which can be subdivided into three different generations (Table 4; Figs. 2D, E). The first generation (Opx I) ranges in X_{Mg} between, 0.42 and 0.43 and the second generation (Opx II) between 0.54 and 0.63 (Table 4). A third generation (Opx III) was observed in a few samples where it forms symplectites with anorthite-rich plagioclase, due to the breakdown of garnet. Orthopyroxene- and plagioclase-bearing symplectites are indicative reaction textures for UHT metamorphic conditions (Figs. 2D, E; Kelsey, 2008). The chemical composition of orthopyroxene (Opx III) in the symplectite is similar (Table 4) in X_{Mg} ratio to orthopyroxene of the second generation (Opx II). The Al_2O_3-content varies from 0.39 to 2.45 wt. % (Table 4).

Pigeonite could only identified in sample HS88. This is a very rare mineral in granulites but has also been described in granulites from other localities (Bucher and Frost, 2006). It forms subidiomorphic grains of the same size as orthopyroxene of the second generation (Opx II). The X_{Mg} ratio is about 0.53, the Al_2O_3 content is lower than in orthopyroxene of the second generation and is up to 0.28 wt. %. In contrast to orthopyroxene, pigeonite in this sample shows an up to five times higher concentration in CaO, which is 2.52 wt. % (Table 4).

Clinopyroxene was occasionally found in the charnockitic gneisses. It either forms subidiomorph grains, or occurs as rims around orthopyroxene (Opx II) (Figs 2F, H), or appears as inclusions in garnet coronas. X_{Mg} varies from 0.66 to 0.78, the Al_2O_3-content is 0.7–5.3 wt.%, and the Na_2O-content is up to 0.7 wt.% (Table 5).

Plagioclase and K-feldspar show typical antiperthitic (K-feldspar lamellae in plagioclase) and perthitic (plagioclase lamellae in K-feldspar) textures. X_{Kfs} in K-feldspar ranges between 0.9 and 0.97. The X_{An} in plagioclase ranges between 0.46 and 0.49 for plagioclase occur as equilibrium phase (Tables 6, 7). A second group of plagioclase is intergrown with orthopyroxene in symplectites, and is enriched in X_{An}, ranging between 0.50 and 0.59; it is only it is up to 0.79 in sample HS92 (Tables 6, 7).

Biotite was only found in small amounts. X_{Mg} is varies between 0.58 and 0.82, the TiO_2-content is 3.29 - 5.55 wt. %, and the F-content is up to 1.88 wt.% (Supplement Table 2).

Amphibole typically forms small, greenish, crystals (0.5-1 mm), but in rare cases also occurs as small rims (<0.1 mm) on the margin of clinopyroxene. The chemical composition varies significantly from sample to sample with X_{Mg} ranging from 0.35 to 0.66; the TiO_2 concentration varies between 0.22 and 2.35 wt.%, the F-content is up to 0.79 wt.%, and Cl is up to 1.09 wt.% (Supplement Table 3). According to Leake et al. (1997) these amphiboles are classified as tschermakite to (ferro-) pargasite.

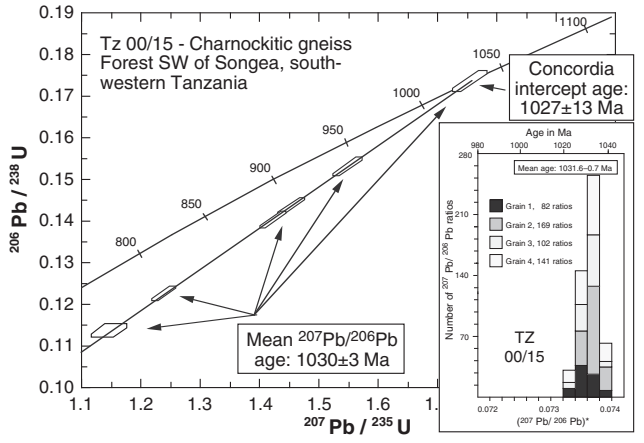

Fig. 4. Concordia diagram showing analytical data for SHRIMP II analyses of zircons from charnockitic gneiss sample Tz 00/15. Error polygons for each analysis are defined by standard errors in $^{207}Pb/^{235}U$, $^{206}Pb/^{238}U$ and $^{207}Pb/^{206}Pb$. Inset shows histogram with distribution of radiogenic lead isotope ratios derived from evaporation of four single zircons from same sample, integrated from 494 ratios.

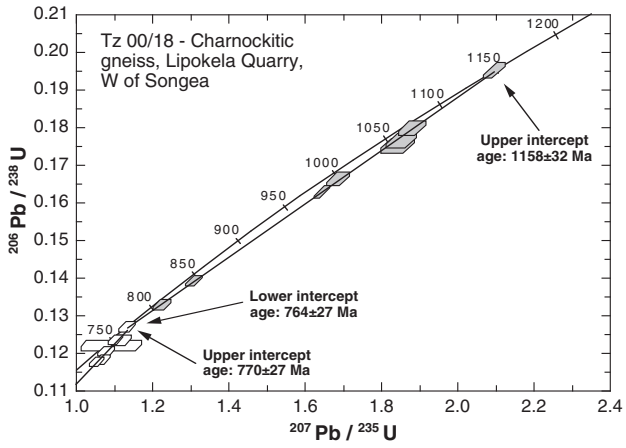

Fig. 5. Concordia diagram showing analytical data for SHRIMP RG analyses of zircons from charnockitic gneiss sample Tz 00/18. Error polygons as in Fig. 6. Core analyses (gray pattern) reflect inheritance whereas rim analyses (open polygons) are interpreted to reflect magmatic emplacement. For explanation see text.

Fe-Ti-oxide phases are common in all rock types. Typically, three different mineral phases can be distinguished, namely pure hematite and ilmenite and a Ti-rich hematite with approx. 10-20 wt.% TiO_2 (Supplement Table 4). Exsolution of hematite and ilmenite in ilmenite and Ti-rich hematite, respectively, has been observed. The Mn-content in ilmenite is up to 0.82 wt.%, whereas Mg is between 0.88 and 2.18 wt.% (Supplement Table 4). The investigated scapolites are mizzonites with high Ca and CO_2 concentrations and show high birefringence.

3.4. Undeformed granitoid rocks

Large outcrops of unfoliated or slightly foliated granitoid rocks occur N and SE of Songea. The mineral assemblage comprises Qtz - Kfs - Pl - Bt ± Am ± Czo/Aln ± Ms ± Fe-Ti oxides. Large perthitic feldspar is common in these rocks (Table 2). These granites are intruded into amphibolite-facies metapelites.

4. Zircon geochronology

Zircon separation procedures, CL imaging and analytical techniques are summarized in the Appendix. Sample Tz 00/15 is a massive, dark gray charnockite, interlayered with garnet-pyroxene gneisses and was collected in a forest west of Songea (Fig. 1B). It contains the mineral assemblage orthopyroxene (Opx) - biotite (Bt) - plagioclase (Pl) - K-feldspar (Kfs) – quartz (Qtz). Zircons are clear to gray-olive, long-prismatic and slightly rounded at their terminations, typical of igneous grains subjected to metamorphic "corrosion" during high-grade metamorphism (Hoskin and Black, 2000; Kröner et al., 1994; Silver, 1969). Cathodoluminescence (CL) images revealed no visible zonation and no inherited cores. Six grains were analyzed on the Perth SHRIMP II and produced one concordant and five variably discordant data points (Supplement Table 5, Fig. 4) that are well aligned in the Concordia diagram and define a mean $^{207}Pb/^{206}Pb$ age of 1030 ± 3 Ma. Recent Pb-loss is indicated, and a regression line through all six analyses and the origin (MSWD = 0.27) yielded an upper concordia intercept age of 1027 ± 13 Ma (Fig. 4). Five additional grains were evaporated individually of which four have identical $^{207}Pb/^{206}Pb$ ratios with a mean age of 1031.6 ± 0.7 Ma (Supplement Table 6, Fig. 4, inset). This is identical to, but more precise than, the SHRIMP age, and we interpret this to most closely approximate the time of emplacement of the charnockite precursor. Two of the evaporated grains produced anomalously high $^{207}Pb/^{206}Pb$ ratios corresponding to mean ages of 1370.0 ± 1.3 and 1600.4 ± 0.8 Ma respectively (Supplement Table 6, not shown in Fig. 4) that we consider to reflect zircon xenocrysts inherited from the source terrain of the original intrusion.

Sample Tz 00/18 is dark, massive, fine-grained charnockitic gneiss collected from Lipokela Quarry along the main road west of Songea (Fig. 1B). The rock-forming minerals are orthopyroxene (Opx), plagioclase (Pl), K-feldspar (Kfs), amphibole (Am) and quartz (Qtz). In

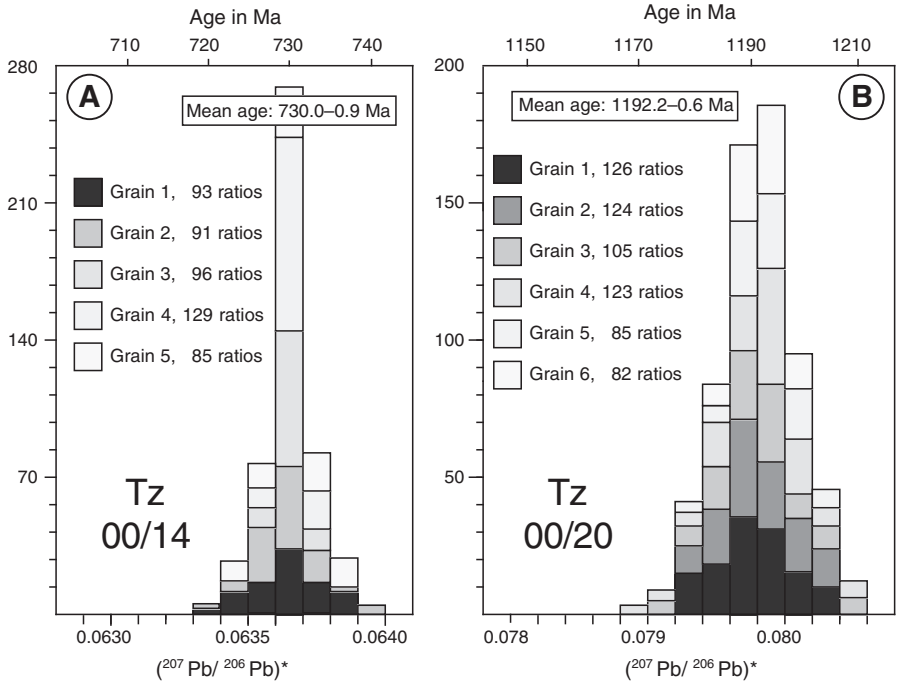

Fig. 6. Histograms showing distribution of lead isotope ratios derived from evaporation of zircons from samples around Songea, SW Tanzania. (A) Spectrum for 5 grains from coarse-grained granite-gneiss sample Tz 00/14, quarry SE of Songea, integrated from 494 ratios (B) Spectrum for 6 grains from migmatitic granite-gneiss sample Tz 00/20, Mpitimbi quarry, S of Songea, integrated from 645 ratios.

the vicinity of the outcrop numerous NE-SW striking quartz veins within minor shear zones occur in the quarry. The zircons are pink, long-prismatic and rounded at their terminations, and CL imagery shows well-defined medium to light gray rims around dark gray cores. These rims occasionally have tail-like forms and represent overgrowths. Fifteen spots were analyzed on the Stanford SHRIMP RG and yielded variable results. The core data define one concordant analysis at 1148 ± 15 Ma, whereas the remaining results are variably discordant (Supplement Table 5) but can be fitted to a discordia line (MSWD = 0.43) whose upper concordia intercept is anchored at the 1148 Ma point, whereas the lower intercept is anchored at a concordant rim analysis of 770 ± 30 Ma (Fig. 5). The resulting upper intercept age is 1158 ± 32 Ma. The remaining rim analyses are slightly discordant but are aligned along a second discordia (MSWD = 0.20) indicating recent Pb-loss and intersecting concordia at 770 ± 27 Ma (Fig. 5). We interpret this pattern in the following way: the discordant analyses defining the upper discordia line in Fig. 5 probably reflect Pb-loss at ~770 Ma and/or a mixture of ~1150 and ~770 Ma material. The overgrowth material formed at ~770 Ma and either reflects zircon growth during a metamorphic or magmatic event. The fact that the overgrowth material has relatively high Th/U ratios and does not exhibit typical CL-features of metamorphic grains argues for the overgrowth to have been produced by a magmatic process, the more so since no high-grade metamorphic event around ~770 Ma is known from this part of East Africa. We are therefore inclined to attribute the ~770 Ma material to a magmatic event during which zircon growth occurred. This makes it likely that the older ~1150 Ma zircon cores represent xenocrysts from a chronologically homogeneous source from which the charnockite precursor was derived by melting at about ~770 Ma. The high-grade event producing the charnockitic mineral assemblage remains undated.

Sample Tz 00/14 is a coarse-grained, reddish, vertically foliated biotite granite-gneiss from a small quarry southeast of Songea. The rock contains streaky, drawn-out melt patches, suggesting that ductile deformation outlasted the peak of metamorphism, but these melt patches have been avoided during sampling. The rock-forming minerals are quartz (Qtz), plagioclase (Pl), K-feldspar (Kfs), biotite (Bt) as well as accessory muscovite (Ms). The zircons are yellow-brown, stubby to long-prismatic and have well rounded terminations. Five grains were evaporated individually and produced a precise mean $^{207}Pb/^{206}Pb$ age of 730 ± 0.9 Ma (Supplement Table 6, Fig. 6A), considered to reflect the time of emplacement of the gneiss protolith.

Sample Tz 00/20 is a gray, fine-grained, layered granite-gneiss collected in the large Mpitimbi Quarry south of Songea. As in the previous case, the rock contains numerous melt patches, and our sample reflects the most homogeneous part of the rock unit. It contains the mineral assemblage quartz (Qtz) - plagioclase (Pl) - K-feldspar (Kfs) - biotite (Bt) and minor titanite (Ttn) and ilmenite (Ilm). Rare metamorphic clinopyroxene (Cpx) was also found. The zircons are long-prismatic to stubby, clear to light yellow-brown and have rounded terminations. Six grains were evaporated individually and yielded a surprisingly old mean $^{207}Pb/^{206}Pb$ age of 1192 ± 0.6 Ma (Supplement Table 6, Fig. 6B) that we interpret to reflect the time of igneous emplacement of the gneiss protolith.

5. Geothermobarometry

Classical geothermobarometry and *P–T* pseudosections have been used to determine the metamorphic history of the metapelites, charnockites and gneisses of the Songea area. In order to estimate peak metamorphic conditions, mineral core- and rim compositions of selected mineral pairs have been used. To calculate fO_2 conditions during metamorphism, Ti-Fe oxides were used. XH_2O (a mixture of H_2O and CO_2) was calculated using the *P–T* values obtained from garnet biotite speedometry. These *P–T* values were used to produce a tally with the H_2O-bearing biotite in/out reaction curve in *P–T* space

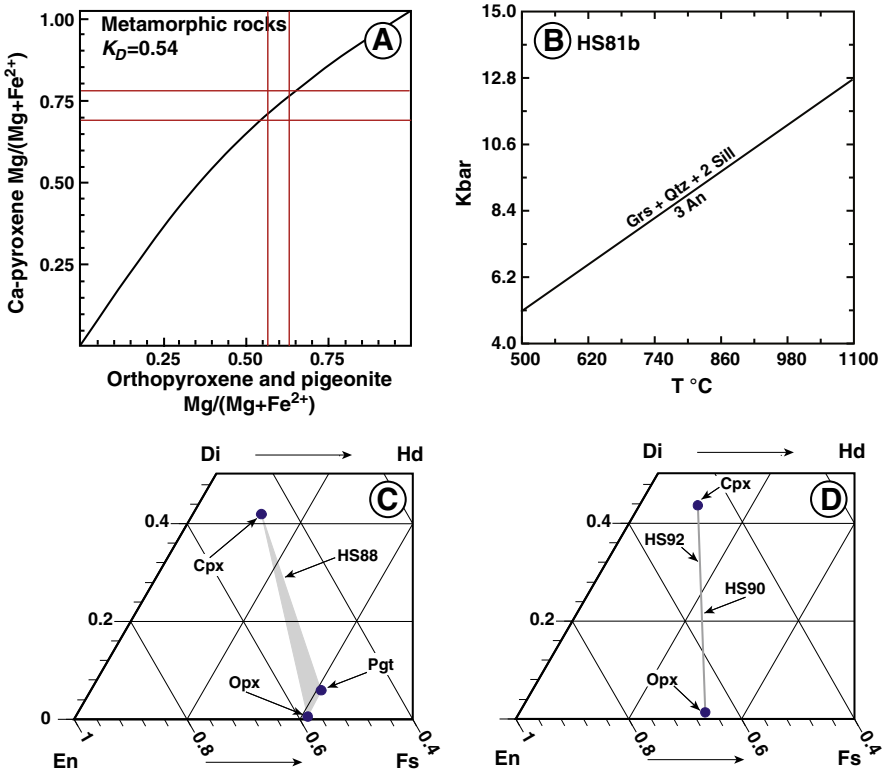

Fig. 7. *P–T* calculations: (A) X_{Ca} in Cpx versus X_{Mg} in Opx and pigeonite diagram showing that the pyroxenes are in equilibrium. (B) GASP barometry for sample HS81b. (C) QUILF thermometry calculation for Opx, Pgt and Cpx pairs of sample HS88. (D) QUILF thermometry calculations for Opx and Cpx pairs of samples HS90 and HS92.

in the computed pseudosections. Similar *P–T* values for both reaction curves could be obtained using an X_{H2O} of 0.7 for the biotite in/out reaction curve in the calculated *P–T* diagrams (Figs. 8A, 10a, 12a, 14a). Four *P–T* pseudosection were calculated to estimate the *P–T* stabilty fields of the different stable mineral assemblages in *P–T* space and to estimate the change in mineral chemical- and volumetric composition in *P–T* space.

5.1. QUILF calculations

The most useful rock type to calculate peak metamorphic temperatures were the charnockites, collected from Lipokela Quarry and close to Litetema, about 30 km to the west of Songea (Fig. 1B). These samples contain orthopyroxene, pigeonite and clinopyroxene. Several thermometers exist for this coexisting mineral assemblage (Frost and Lindsley,

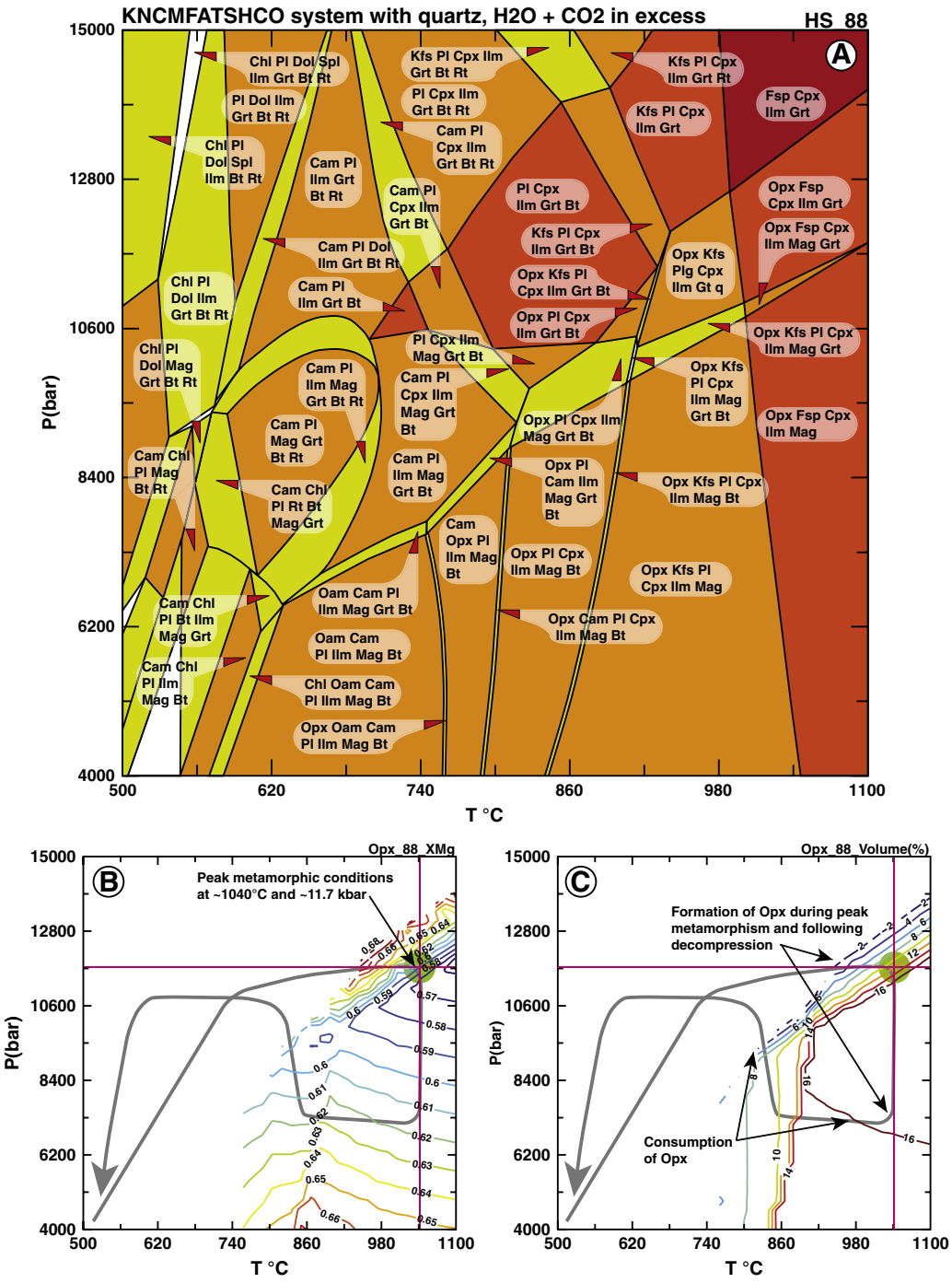

Fig. 8. (a) *P–T* pseudosection for sample HS88 in the KNCMFATSHCO system. Peak metamorphic mineral assemblage is Opx, Cpx, Fsp, Grt, Ilm and Qtz (b) Variation in X_{Mg} in Opx for sample HS88. Red cross with green dot marks peak metamorphic conditions and the gray-colored slope represent the calculated *P–T* path. (c) Volumetric calculation for Opx in sample HS88 shows that Opx grew during peak metamorphism and later became consumed during near-isothermal decompression with decreasing temperature and increasing pressure along the calculated *P–T* path. (For interpretation of the references to color in this figure legend, the reader is referred to the web version of this article.)

1992; Lindsley and Frost, 1992; Saxena et al., 1968). To test whether the analyzed orthopyroxene, pigeonite and clinopyroxene are in equilibrium, the X_{Mg} ratios of these minerals were plotted against each other and were checked whether they match the K_D line of 0.54 for metamorphic rocks (Saxena et al., 1968; Fig. 7A). To calculate the peak metamorphic temperature at which orthopyroxene, pigeonite and clinopyroxene have been in equilibrium, we used the *QUILF* program (Andersen et al., 1993) and the following thermometers; (1) enstatite component in clinopyroxene and orthopyroxene (EnCpxOpx), (2) enstatite component in clinopyroxene and pigeonite (EnCpxPig),

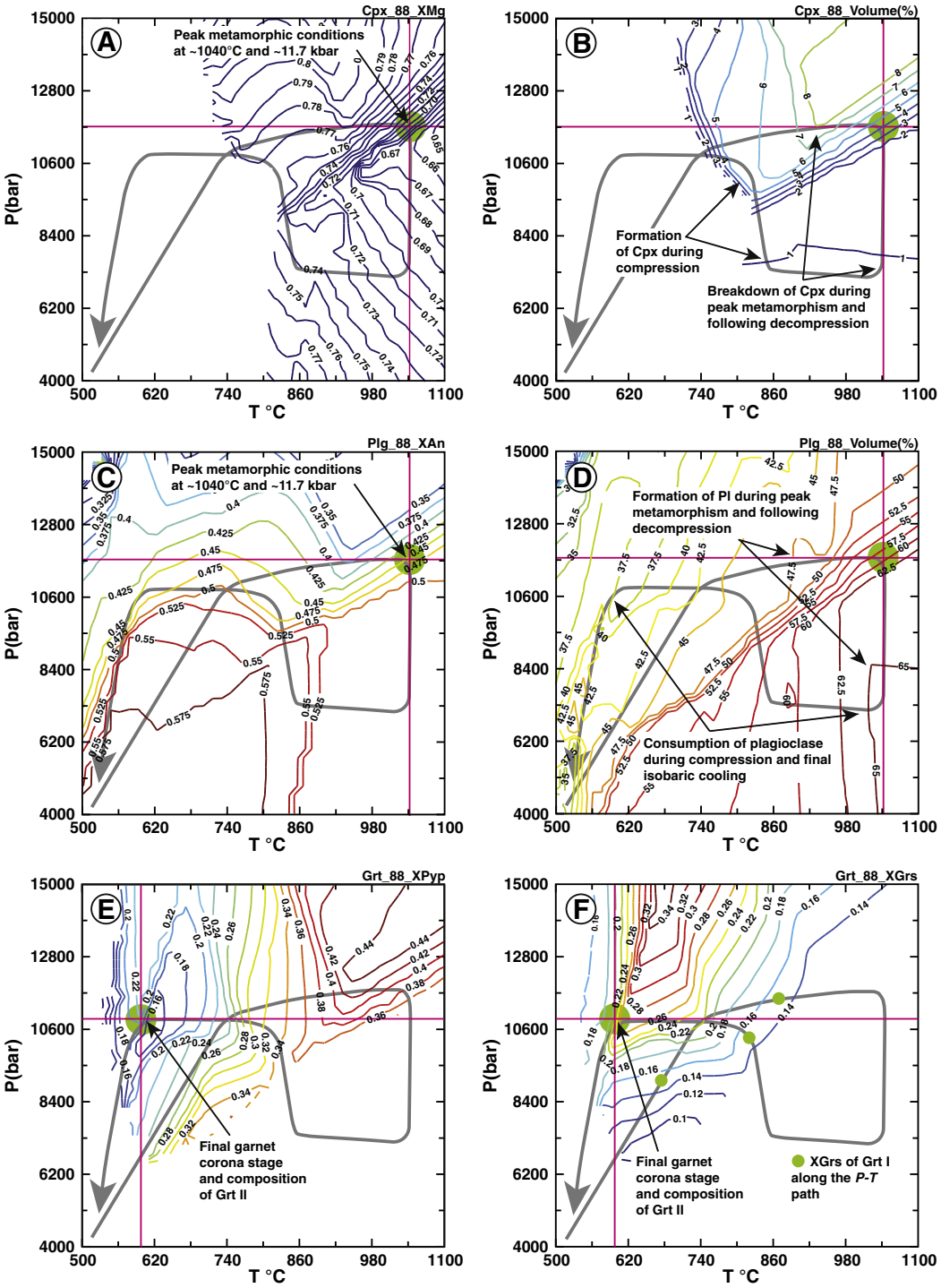

Fig. 9. (A) Variation in X_{Mg} in Cpx of sample HS88. Red cross and green dot show peak metamorphic conditions along the calculated *P–T* path. (B) Volumetric computation for Cpx indicates that it was consumed during peak metamorphism and subsequent decompression and grew with decreasing temperature and increasing pressure in a first phase and was later consumed along the *P–T* path. (C) Diagram showing variation of X_{An} in plagioclase, which is 0.45 during peak metamorphism seen at the calculated *P–T* path. (D) Volumetric calculations of plagioclase indicate that this mineral formed during decreasing pressure and was consumed during isobaric cooling along the *P–T* slope. (E, F) Variations in X_{Pyp} and X_{Grs} after isobaric cooling; red cross with the green dots shows *P–T* conditions after isobaric cooling and garnet corona formation along the *P–T* path. Small green dots are representative of X_{Grs} of Grt I in sample HS88. (For interpretation of the references to color in this figure legend, the reader is referred to the web version of this article.)

and (3) enstatite component in pigeonite and orthopyroxene (EnPigOpx). All three thermometers must yield the same or nearly the same temperature range for the studied rock samples using the *QUILF* program (Andersen et al., 1993). The calculated peak metamorphic temperatures and pressures for sample HS88 range between ~1046 °C, ~11.7 kbar (EnCpxOpx; Fig. 7c) and ~1009 °C, ~11.7 kbar (EnCpxPig and EnPigOpx; Fig. 7c). The variation in the computed peak metamorphic temperature is probably due to variations in Fe-Mg ion exchange during cooling (Bucher and Frost, 2006). Sample HS92 yielded peak metamorphic temperatures and pressures of ~1024 °C and ~11.9 kbar (EnCpxOpx; Fig. 7d). Due to the occurrence of Fe-Ti oxides in sample HS92, the magnetite-hematite and Fe-Ti thermometers were also used and yielded temperatures of 1029 °C and 829 °C, respectively. The calculated fO_2 varies between -11.5 and -11.7. Sample HS90 yielded peak metamorphic temperatures of up to 1020 °C at ~11.5 kbar (EnCpxOpx), and fO_2 is -11.4 (Fig. 7d).

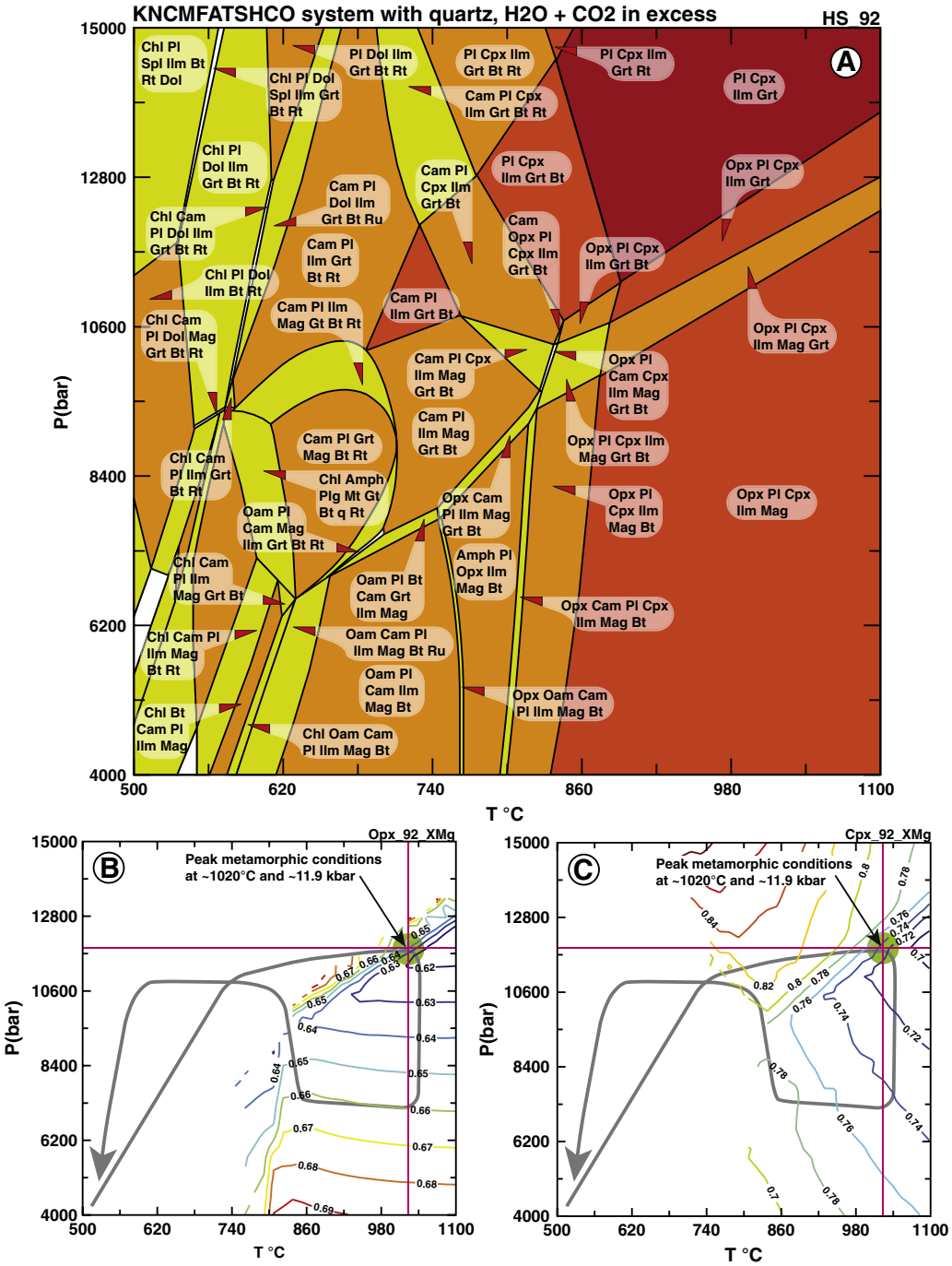

Fig. 10. (A) *P–T* pseudosection computed for sample HS92 in the KNCMFATSHCO system. The UHT garnulite-facies mineral assemblage is Opx, Cpx, Pl, Grt, Ilm and Qtz. (B) Computed variation of X_{Mg} ratio for Opx in sample HS92; Red Cross with green dot marks peak metamorphic conditions for the calculated *P–T* path. (C) X_{Mg} variation in Cpx of sample HS92. (For interpretation of the references to color in this figure legend, the reader is referred to the web version of this article.)

5.2. TWQ calculations

To estimate pressure conditions at peak metamorphic temperatures between ~1000 and ~1050 °C, we used the garnet-sillimanite-plagioclase-quartz geobarometer. The database of Berman and Arranowich (1996) was used for the computation using TWQ 2.0.2.

$$\text{Grossular} + 2\ \text{Sillimanite} + \text{Quartz} = 3\text{Anorthite}(\text{GASP})$$

Sample HS81b was used for barometry because the analyzed garnets (Grt I) grew during prograde metamorphism due to the increase of X_{Pyp} from core to rim and the high X_{Pyp} ratios that are indicative of granulite–facies metamorphism (Table 3). The calculated pressures for gneiss sample HS81 at the above temperatures are up to ~12 kbar at ~1050 °C (Fig. 7B).

5.3. PerPleX calculations

Four *P–T* pseudosections were calculated using the PerPleX toolbox (Connolly, 1990), employing the PerPleX JS 6.6.6 Macintosh version and datafile HP02ver.dat (Connolly, 2005). In order to obtain the physiochemical information in the *P–T* range of interest, we modified and simplified the solution model files provided by the PerPleX toolbox. This means that non-existing endmembers, or endmembers which occur only in minor volumes, were removed from the solution and from the projection space. The modified solution files for orthopyroxene and clinopyroxene were then treated as ideal solutions because ideal mixing of orthopyroxene and clinoyroxene can be expected at temperatures of ~1000 °C. The modified solution file for garnet is a simplified solution model, because only the pyrope, grossular and almandine endmembers are of interest under granulite-facies conditions. The ternary feldspar model of Fuhrman and Lindsley (1988) was used for the charnockitic gneisses, and a binary plagioclase solution model was used to calculate the pseudosection for the gneiss (Newton et al., 1981). We used the models of Andersen and Lindsley (1988) to compute the Fe–Ti oxide phases in *P–T* space. One ortho- and one clino-amphibole model was used for the computation (Dale et al., 2000; Holland and Powell, 1998). The solution models for biotite, chlorite, cordierite and dolomite were also simplified and were taken from the database of Holland and Powell (1998).

5.4. Pseudosection HS88

Sample HS88 is a charnockitic gneiss that contains some older garnet relicts (Grt I) that formed during prograde metamorphism and younger garnet rims/coronas (Grt II; Fig. 2F) that formed during retrograde metamorphism, respectively. Orthopyroxene (Opx II) and clinopyroxene occur as equilibrium phases. The *P–T* pseudosection was computed in the KNCMFATSHCO system and contains 54 phase fields (Fig. 8A). The following 12 solution models and phases were used for the computation: orthopyroxene (Opx), clinopyroxene (Cpx), garnet (Grt), feldspar (Fsp), biotite (Bt), anthophylite (Oam), clinoamphibole (Cam), chlorite (Chl), dolomite (Dol), spinel (Spl), ilmenite-hematite (Ilm), magnetite-ulvöspinel (Mag), rutile (Rt) and quartz (Qtz). The solution models have been simplified as described above. The bulk composition is: $Na_2O = 2.306$; $MgO = 4.013$; $Al_2O_3 = 16.601$; $SiO_2 = 50.425$; $K_2O = 1.318$; $CaO = 6.209$; $TiO_2 = 2.216$; FeO: = 12.548; $O_2 = 0.559$ and $X_{H2O} = 0.7$. The peak metamorphic mineral assemblage is orthopyroxene, clinopyroxene, garnet, feldspar, ilmenite and quartz (Fig. 8A). The resulting peak metamorphic conditions from our computation is ~1040 °C and ~11.7 kbar, using the X_{Mg} ratios of ~0.58 in orthopyroxene (Fig. 8B; Table 4) and ~0.70 in clinopyroxene, respectively (Fig. 9A; Table 5). The peak metamorphic conditions calculated from PerPleX excellently agree with the results of the *QUILF* calculations (Figs. 7C; Tables 4, 5). According to our computations, orthopyroxene grew during peak metamorphism and throughout post-peak decompression and afterwards became consumed during compression and cooling during the following garnet corona growth phase along the retrograde *P–T* path (Fig. 8C). Clinopyroxene was consumed during the peak metamorphic phase and breakdown finally during isothermal decompression (Fig. 9B). Afterwards, clinopyroxene grew due to increasing pressure and was later consumed due to decreasing temperatures (Fig. 9B). The anorthite component in plagioclase was ~0.45 at peak metamorphic conditions (Fig. 9C; Table 6), and plagioclase formed during peak metamorphism and subsequent decompression and was later consumed during retrogression (Fig. 9D). According to our PerPleX computation, the analyzed garnet in sample HS88 was not in equilibrium with orthopyroxene and clinopyroxene during peak metamorphism. These garnets were stable at lower *P–T* conditions of ~600 °C and ~10.9 kbar, which reflects the formation of garnet coronas due to isobaric cooling (Figs. 9E, F & Supplement Fig. 1a, b; Table 3). The observed prograde garnet (Grt I) and orthopyroxene (Opx I) in the charnockite could not be projected into the calculated *P–T* space because the whole-rock composition used for the pseudosection represents the bulk rock chemistry of the last snapshot of metamorphism in an allochemical system and is therefore not representative of prograde metamorphism that occurred during an earlier phase.

5.5. Pseudosection HS92

Sample HS92 is a charnockitic gneiss containing garnet only as a corona phase (Grt II). Orthopyroxene (Opx II) occurs as an equilibrium phase and in orthopyroxene (Opx III) – plagioclase-bearing symplectites that formed due to the consumption of a former no longer existing garnet (Grt I). Clinopyroxene also occurs as an equilibrium phase. The *P–T* pseudosection was calculated in the KNCMFATSHCO system and contains 53 phase fields (Fig. 10A). We used the following 12 solution models and phases for the PerPleX computation: Orthopyroxene (Opx), clinopyroxene (Cpx), garnet (Grt), feldspar (Fsp), biotite (Bt), anthophylite (Oam), clinoamphibole (Cam), chlorite (Chl), dolomite (Dol), spinel (Spl), ilmenite-hematite (Ilm), magnetite-ulvöspinel (Mag), rutile (Rt) and quartz (Qtz). The used bulk composition is: $Na_2O = 2.633$; $MgO = 3.269$; $Al_2O_3 = 16.903$; $SiO_2 = 50.348$; $K_2O = 0.509$; $CaO = 7.165$; $TiO_2 = 0.815$; $FeO = 7.860$; $O_2 = 0.350$ and $X_{H2O} = 0.7$. According to our PerPleX computation, the peak metamorphic mineral assemblage is orthopyroxene, clinopyroxene, garnet, plagioclase, ilmenite and quartz (Fig. 10A). The calculated peak metamorphic temperature from our PerPleX computation is ~1020 °C, and the corresponding pressure is ~11.9 kbar. This peak metamorphic conditions has been determined using X_{Mg} ratios in orthopyroxene of ~0.63 (Fig. 10B; Table 4) and in clinopyroxene of ~0.74, respectively (Fig. 10C; Table 5). The X_{Mg} values during peak metamorphism from our PerPleX computation are the same as the calculated ratios from the EPMA analyses that were used for the *P–T* estimations with *QUILF* (Fig. 7D; Tables 4, 5). Our calculations show that orthopyroxene formed during peak metamorphism and the following symplectite phase and was consumed due to compression along the retrograde *P–T* path and finally during subsequent isobaric cooling during the garnet corona growth phase (Supplement Fig. 1c). In contrast, clinopyroxene was consumed during peak metamorphism and the following symplectite phase. It grew later again due to compression and was subsequently consumed during decreasing temperature (Supplement Fig. 1d). The anorthite component in plagioclase was ~0.5 at peak metamorphic conditions (Fig. 11A; Table 7) and formed during the symplectite stage and consumed along the retrograde *P–T* slope (Fig. 11B). The occurrence of plagioclase with a X_{An} ratio of up to 0.79 in the symplectite is an unresolved problem and requires further study. According to our PerPleX computation, the analyzed garnet in sample HS92 is not in equilibrium during peak metamorphism with orthopyroxene and clinopyroxene. It was stable at lower *P–T* conditions at about 680 °C and 10.6 kbar, which is indicative for the formation of garnet coronas (Figs. 11 C-E; Supplement Fig. 1e; Table 3).

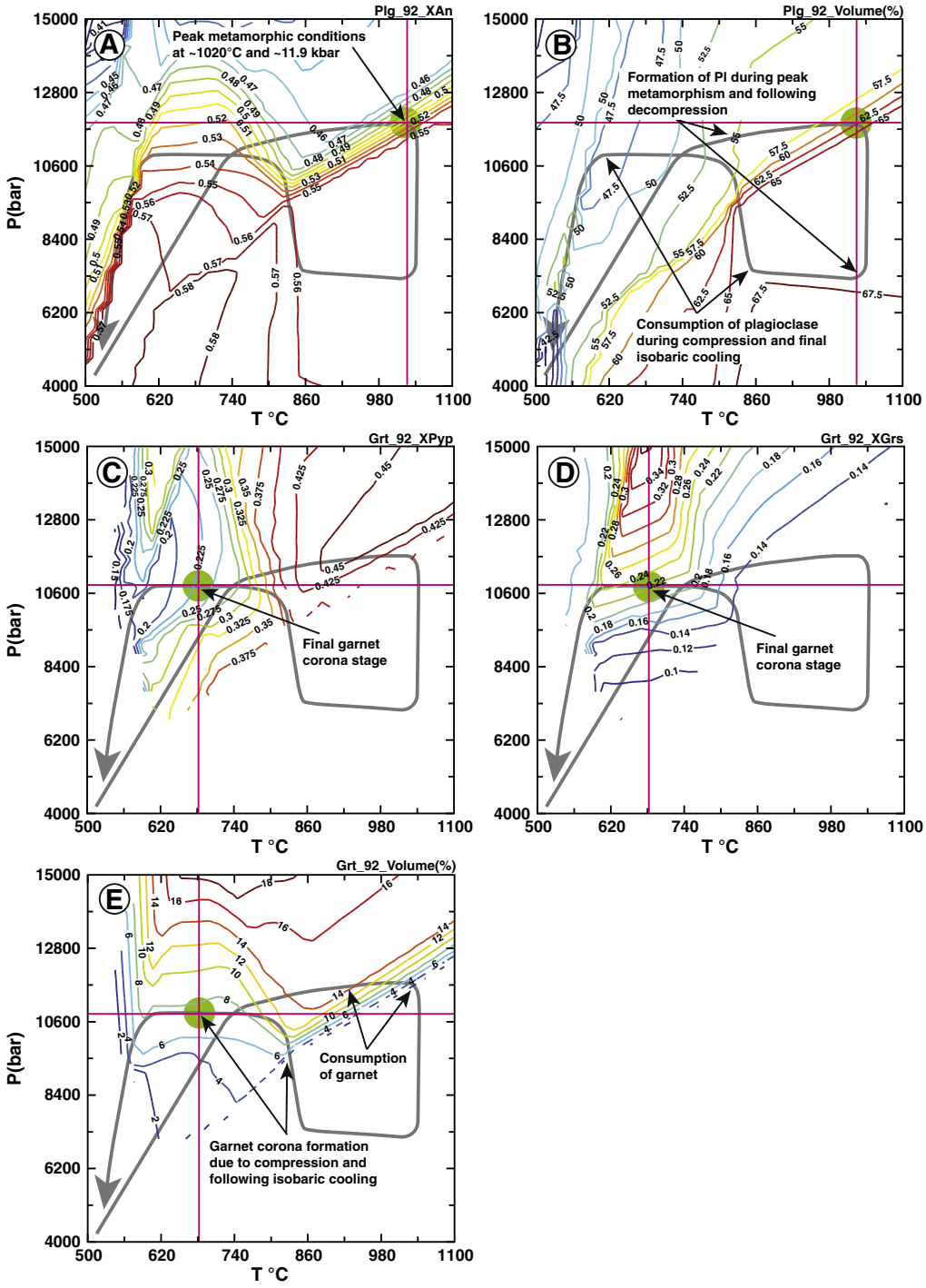

Fig. 11. (A) Distribution of X_{An} in plagioclase of sample HS92 along the *P–T* path. Red cross and green dot mark peak metamorphic conditions. (B) Volumetric calculation of plagioclase in sample HS92 shows that this mineral formed during the symplectite phase and was consumed with decreasing temperature along the calculated *P–T* path. (C–D) diagrams showing variation in X_{Pyp} and X_{Grs} for sample HS92. Red Cross and green dots mark the phase of garnet corona formation caused by isobaric cooling at ~680 °C and ~10.7 kbar at the calculated *P–T* path. (E) Volumetric calculations for garnets from sample HS92 show that garnet grew with decreasing temperature and increasing pressure and was consumed with increasing *P–T* conditions along the computed *P–T* path. (For interpretation of the references to color in this figure legend, the reader is referred to the web version of this article.)

5.6. Pseudosection HS83:

Sample HS83 is a charnockitic gneiss that also contains garnet relics (Grt I); orthopyroxene (Opx II) occurs as an equilibrium phase and in orthopyroxene (Opx III) – plagioclase - bearing symplectites. Clinopyroxene occurs as an equilibrium phase. The *P–T* pseudosection was computed in the KNCMFATSHCO system and contains 47 phase fields (Fig. 13A). The following 12 solution models and phases were used for the calculation: Orthopyroxene (Opx), clinopyroxene (Cpx), garnet (Grt), feldspar (Fsp), biotite (Bt), anthophylite (Oam), clinoamphibole (Cam), chlorite (Chl), dolomite (Dol), spinel (Spl), ilmenite-hematite (Ilm), magnetite-ulvöspinel

(mag), rutile (Rt) and quartz (Qtz). The used bulk composition is $Na_2O = 1.239$; $MgO = 6.947$; $Al_2O_3 = 12.037$; $SiO_2 = 42.933$; $K_2O = 0.294$; $CaO = 11.689$; $TiO_2 = 2.979$; $FeO = 15.902$; $O_2 = 0.699$ and $X_{H2O} = 0.7$. According to our PerPleX calculation, the peak metamorphic mineral assemblage is orthopyroxene, clinopyroxene, garnet, plagioclase, ilmenite and quartz (Fig. 12A). At peak metamorphic conditions at about 1020 °C and about 12 kbar, the X_{Mg} in orthopyroxene is ~ 0.65 (Fig. 12B) and ~0.74 in clinopyroxene (Fig. 12C). The computed X_{Mg} values with PerPleX are in good agreement with the measured and calculated ratios from the EPMA analyses that were used for the *QUILF* calculations (Tables 4, 5). According to our computations, orthopyroxene grew during peak metamorphism and the subsequent symplectite phase and was consumed due to compression within the orthopyroxene stability field (Supplement Fig. 1f), whereas clinopyroxene was consumed during isothermal decompression and formed during compression and was subsequently consumed during decreasing temperature due to

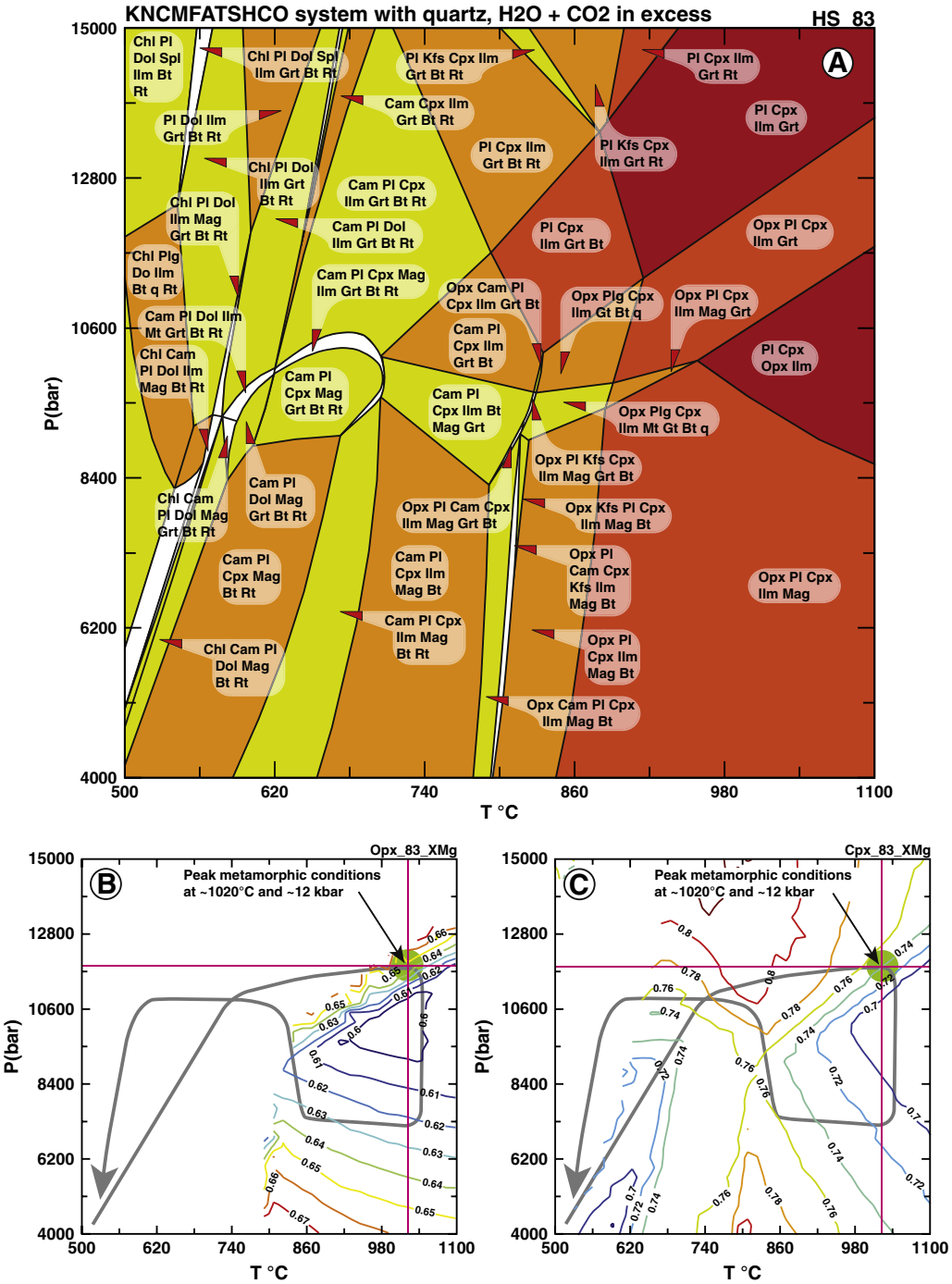

Fig. 12. (A) Calculated *P–T* pseudosection for sample HS83 in the KNCMFATSHCO system. The UHT garnulite-facies mineral assemblage is Opx, Cpx, Pl, Grt, Ilm and Qtz. (B) Diagram showing variation in X_{Mg} ratio in Opx for sample HS83; Red Cross with green dot marks peak metamorphic conditions. (C) Variation of X_{Mg} ratio in Cpx from sample HS83; Red Cross with green dot marks peak metamorphic conditions. (For interpretation of the references to color in this figure legend, the reader is referred to the web version of this article.)

isobaric cooling (Supplement Fig. 2a). The anorthite component in plagioclase was about 0.55 at peak metamorphic conditions (Fig. 13A) and plagioclase grew during the symplectite phase and was consumed during retrograde metamorphism (Fig. 13B). Due to our PerPleX computation, the analyzed garnet in sample HS83 is not in equilibrium with orthopyroxene and clinopyroxene during peak metamorphism. The analyzed garnet relics in sample HS83 were stable at lower *P–T* conditions at about 740 °C and 10.7 kbar and are interpreted as a

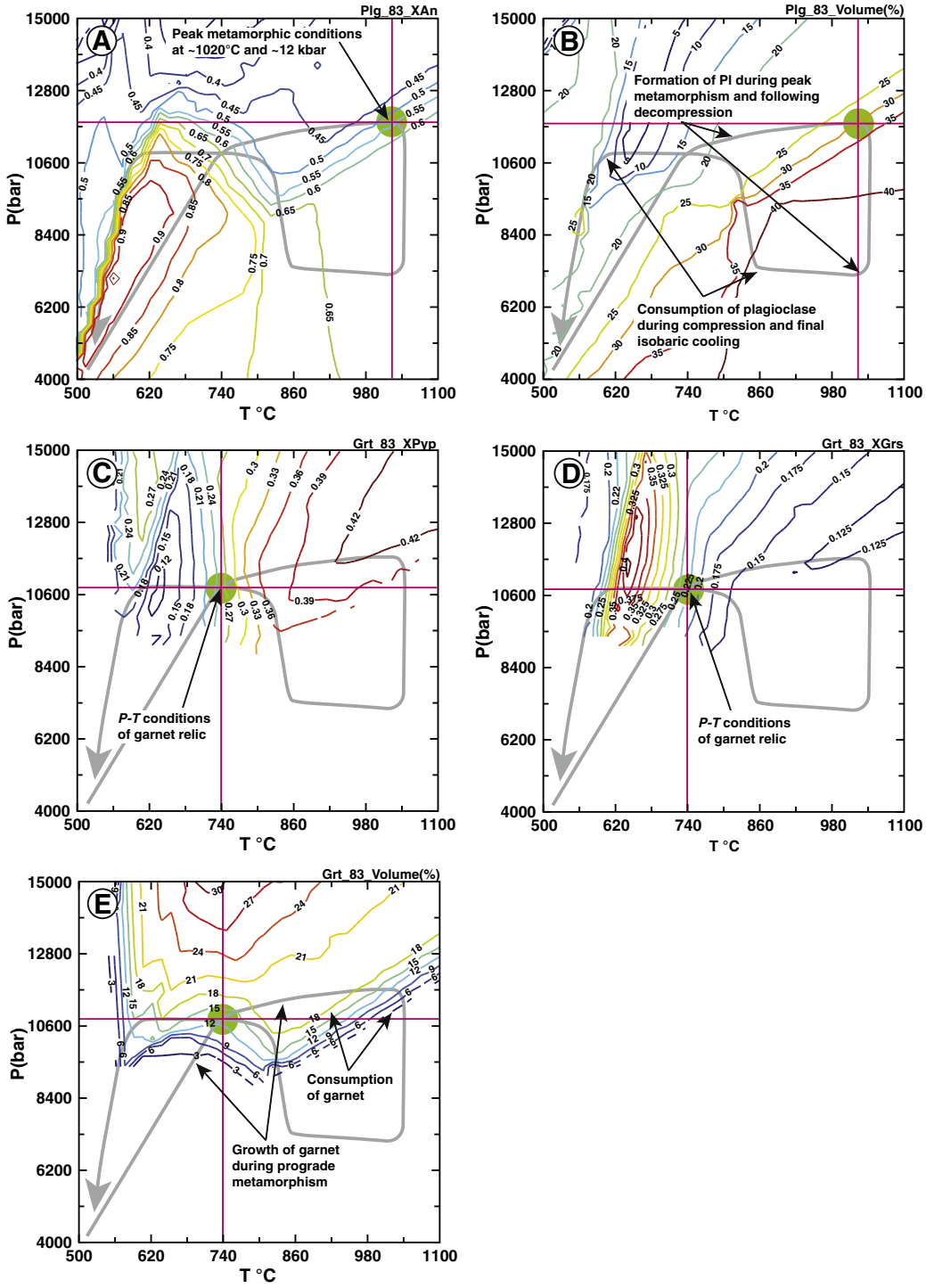

Fig. 13. (A) Diagram showing variation of $X_{An} = 0.55$ in plagioclase during peak metamorphism; red cross with green dot marks peak metamorphic conditions. (B) Volumetric calculations of plagioclase indicate that this mineral formed along the prograde *P–T* path and was consumed during the symplectite phase along the retrograde *P–T* path. (C–D) Diagrams showing variation in X_{Pyp}, and X_{Grs} for sample HS83. Red cross with green dots marks *P–T* conditions for garnet from this particular sample at ~740 °C and ~10.7 kbar. (E) Volumetric calculations for garnets show that this mineral formed during compression and subsequent isobaric cooling along the computed *P–T* path. (For interpretation of the references to color in this figure legend, the reader is referred to the web version of this article.)

relic from garnet (Grt I) that has grown during prograde metamorphism and was later consumed during retrogression (Figs. 13C-E; Supplement Fig. 2b; Table 3).

5.7. Pseudosection HS82

Sample HS82 is an orthogneiss that contains garnet as an equilibrium phase. The *P–T* pseudosection was computed in the KNCMFATSHCO system and includes 37 phase fields (Fig. 14A). The following 13 solution models and phases were used for the computation: orthopyroxene (Opx), cordierite (Crd), garnet (Grt), plagioclase (Pl), K–feldspar (Kfs), biotite (Bt), kyanite (Ky), sillimanite (Sil), dolomite (Dol), ilmenite-hematite (Ilm), magnetite-ulvöspinel (Mag), rutile (Rt) and quartz (Qtz). The solution models were modified as described above. The used bulk composition is: Na_2O = 2.110; MgO = 2.627; Al_2O_3 = 17.674; SiO_2 = 58.508; K_2O = 6.415; CaO = 1.580; TiO_2 = 0.777; FeO = 6.293; O_2 = 0.280 and X_{H2O} = 0.7. The peak metamorphic mineral assemblage is garnet, plagioclase, K-feldspar, ilmenite,

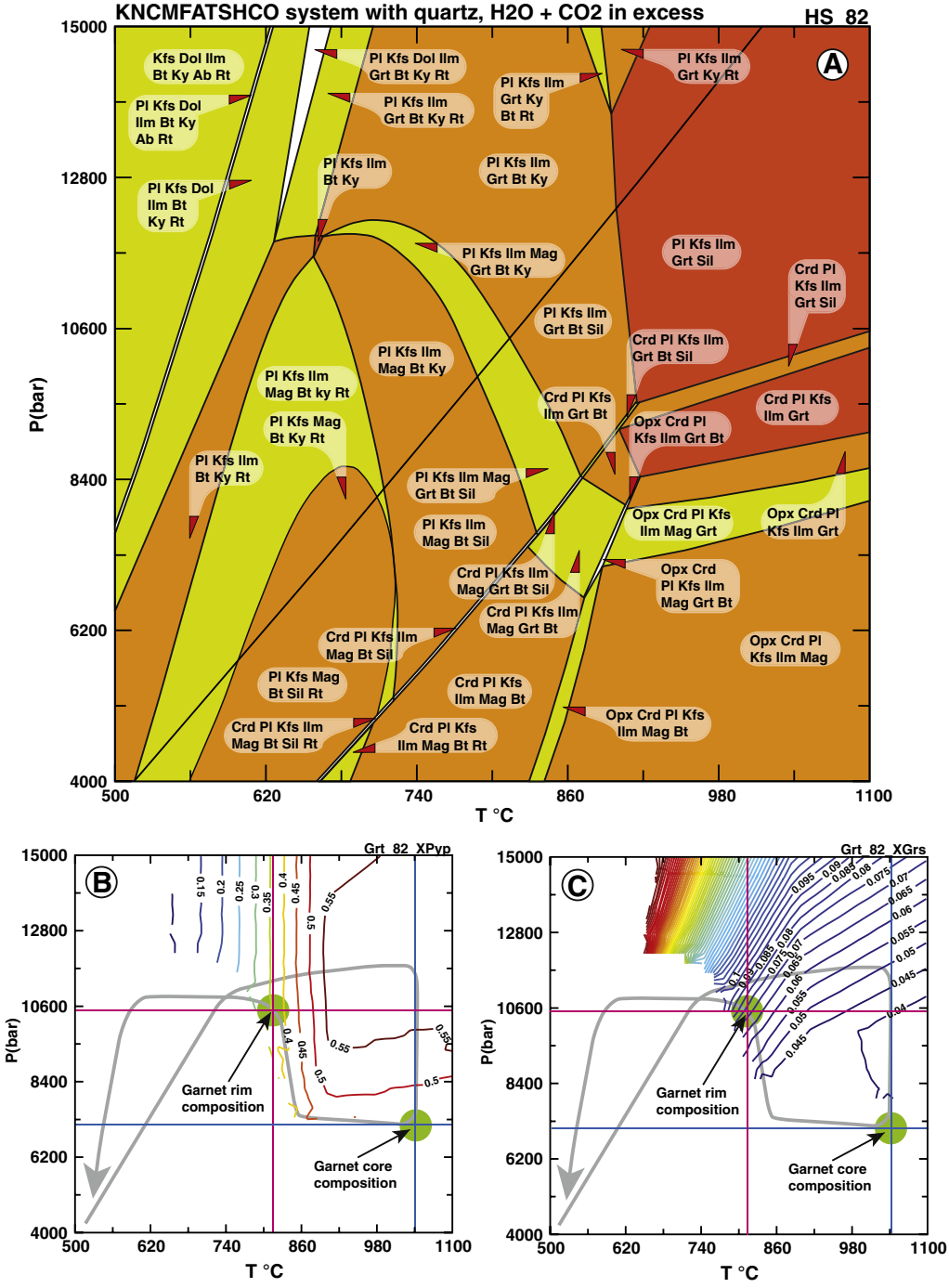

Fig. 14. (A) Computed *P–T* pseudosection for sample HS82 in the KNCMFATSHCO system. The high-grade granulite-facies mineral assemblage is Pl, Kfs, Grt, Ilm and Qtz. (B–C) Diagrams show variations in X_{Pyp} and X_{Grs} ratios and therefore core rim relationships. Blue cross with green dots marks *P–T* conditions for garnet cores, and red cross with green dots shows *P–T* conditions for garnet rims along the computed *P–T* path. (For interpretation of the references to color in this figure legend, the reader is referred to the web version of this article.)

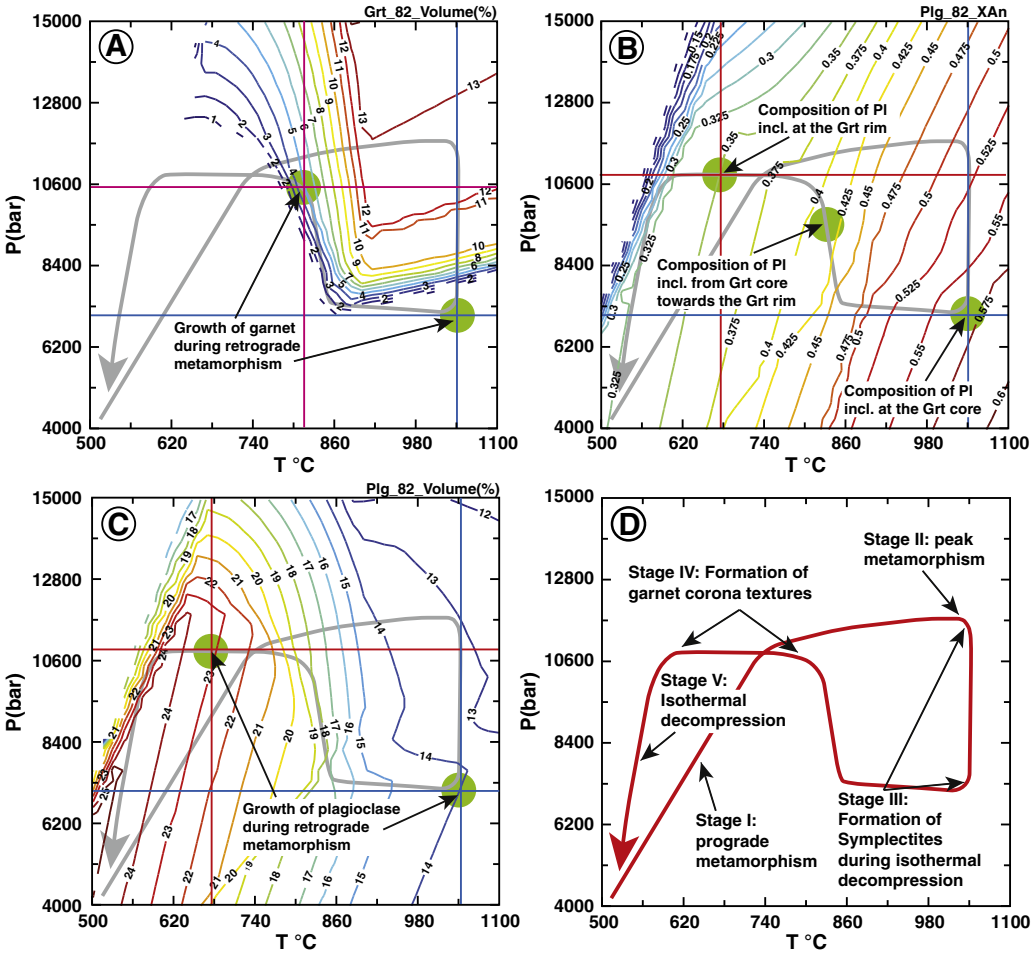

Fig. 15. (A) Volumetric calculations for garnet from sample HS82 show that this mineral grew during retrograde metamorphism along the calculated *P–T* path. (B) Diagram showing decrease in X_{An} in plagioclase inclusions located from core to rim in garnet of sample HS82. X_{An} decreases with decreasing temperature along the retrograde *P–T* path. (C) Volumetric calculations of plagioclase indicate that this mineral grew with decreasing temperature during retrogression. (D) Five-segment *P–T* path for the Songea area. Segment I represents prograde metamorphism. Segment II reflects peak metamorphic conditions at ~1050 °C and ~12 kbar. Segment III marks the formation of orthopyroxene- and plagioclase-bearing symplectites, caused by the breakdown of garnet due to isothermal decompression. Segment IV reflects formation of garnet coronas during isobaric cooling. Segment V shows strong decompression during amphibolite-facies conditions.

sillimanite and quartz (Fig. 14A). In this sample the garnet rim composition together with the plagioclase composition at the rim yielded higher *P* and lower *T* conditions than garnet core compositions with plagioclase compositions from inclusions located in the garnet core. Using the $X_{Pyp/Alm/Grs}$ ratios at the garnet core and rim (Table 3) and comparing it with our PerPleX computation shows how the temperature conditions decreased from the core to the rim in garnet of sample HS82 (Figs. 14B, C, Supplement Fig. 2c). The same feature can be seen in the decrease of the anorthite component in plagioclase inclusions located from core to rim in garnet. The X_{An} ratios in plagioclase inclusions located at the core of the garnet are 0.57, for plagioclase inclusion located towards the rim of the garnet the X_{An} is 0.41 and, finally, plagioclase inclusion located at the rim of garnet the X_{An} is 0.35. Linking the $X_{Pyp/Alm/Grs}$ and X_{An} ratios to *P–T* conditions shows how garnet and plagioclase in sample HS82 grew during retrograde metamorphism (Figs. 14B, C; 15A-C; Supplement Fig. 2c; Tables 3, 6).

6. Metamorphic textures and *P–T* loop

Classical geothermobarometry, computed pseudosections, mineral compositions measured with EPMA, calculated mineral compositions, volumetric calculations, and reaction textures observed in thin section have all been used to construct the *P–T*-loop for the granulite-facies rocks of the Songea area. Peak metamorphic conditions with temperatures of up to ~1050 °C and pressures up to ~12 kbar were obtained.

6.1. Reaction textures constraining different sections on the prograde and retrograde parts of the calculated P–T loop

Prograde P–T path: Mineral relicts of the prograde *P–T* path of the mafic to intermediate charnockites were found in a few samples. In sample HS88 hypersthene (Opx I) with an X_{Mg} ratio of ~0.43 was identified that probably formed at lower *P–T* conditions during prograde metamorphism (Table 4). Garnet relics (Grt I) could be identified in samples HS88 and HS83 (Figs. 2F, 3D; Table 3). We interpret the existence of these garnet relics as remnants of former garnet (Grt I) that grew during prograde metamorphism and was partly consumed during isothermal decompression (Fig. 2F). The garnets (Grt I) in samples HS81 and HS81b also provide a record of the prograde *P–T* path. X_{Pyp} is increasing in both samples (Grt I) from core to rim, and this is undoubtedly indicative of prograde metamorphism (Fig. 3C; Table 3).

Peak metamorphism: Peak metamorphic conditions were calculated using orthopyroxene and clinopyroxene pairs for thermometry and using the GASP reaction for barometry. Peak metamorphic conditions are up to ~1050 °C and ~12 kbar (Fig. 15d). The results

from PerPleX computations show similar peak metamorphic conditions. Our calculated temperatures are characteristic of UHT metamorphism.

6.2. Retrograde metamorphism:

The retrograde *P–T* path is characterized by the formation of orthopyroxene – plagioclase - bearing symplectites due to the breakdown of garnet (Figs. 2D, E). Orthopyroxene- and plagioclase-bearing symplectites are reaction textures indicative of UHT metamorphism, which is confirmed by the geothermobarometric calculations (Kelsey, 2008).

Garnet and clinopyroxene were consumed and orthopyroxene and plagioclase grew (Figs. 8C, 9B, D, 11B, E, 13B, E, 15A, C; Supplement Figs. 1b-d, 1f; 2a) due to the reaction

$$\mathrm{Grt} + \mathrm{Cpx} + \mathrm{Qtz} = \mathrm{Opx} + \mathrm{Pl}. \quad (1)$$

Following the symplectitic phase, cooling and compression occurred (Fig. 15D). This part of the retrograde *P–T* path was constructed using garnet (Grt II) (sample HS82) with plagioclase inclusions that occurred as an equilibrium phase during high-grade metamorphism. The garnet of sample HS82 contains plagioclase inclusions located from core to rim and thus record an increase in *P* and a decrease in *T* conditions from core to rim during growth of garnet along the retrograde *P–T* path (Figs. 14B, C; 15A-C; Supplement Fig. 2c). Garnet of sample HS82 also has inclusions of sillimanite that were inherited during compression on the retrograde *P–T* path (Fig. 14A).

At a later stage isobaric cooling occurred and led to formation of garnet (Grt II) corona textures due to the breakdown of orthopyroxene and plagioclase according to the reaction

$$\mathrm{Opx} + \mathrm{Pl} = \mathrm{Grt} + \mathrm{Cpx} + \mathrm{Qtz}. \quad (2)$$

Two types of textures with garnet coronas are shown in Figs. 2D, F, G, namely (a) garnet coronas around orthopyroxene (Figs. 2F, G) and (b) garnet coronas around Fe-Ti-oxides (Figs. 2D, F, G). Wherever garnet grew around orthopyroxene, a small rim of clinopyroxene and a quartz corona around orthopyroxene developed (Fig. 2F). In contrast, coronas around ilmenite/Ti-hematite, do not show quartz and clinopyroxene rims. Instead, garnets are usually full of small Fe- and Fe-Ti-oxide and some clinopyroxene inclusions (Fig. 2D). The relevant reactions producing garnet coronas around orthopyroxene are similar to those that produced the vermicular intergrowth of orthopyroxene and plagioclase (reactions 1 to 2). The vermicular intergrowth of orthopyroxene and plagioclase is explained by destabilized garnet due to isothermal decompression. Garnet coronas were produced by the breakdown of orthopyroxene and plagioclase during retrogression. The formation of garnet coronas is typical of fluid-absent metamorphism, leading to diffusion-controlled reaction structures such as coronas. The computed volumetric calculation supports this assumption. Garnet grew with decreasing temperature, compression and, finally, isobaric cooling (Figs. 11E; 13E; 15A), whereas orthopyroxene and plagioclase became consumed during compression and subsequent isobaric cooling (Figs. 8C; 9D; 11B; 13B; Supplement Figs. 1c, f; 2a). A small amount of clinopyroxene was also produced during retrogression (Figs. 9B) and occurs as clinopyroxene rims around orthopyroxene (Fig. 2F; Supplement Fig. 1d; 2a). These observations are confirmed by the garnet profiles of sample HS81 (Grt II) and the outermost profiles of Grt II through the outermost rims of samples HS81b and HS88 (Figs. 3C, D) where the same $X_{Pyp/Alm/Grs}$ ratios in garnet can be found, as expected, in the garnet corona formation phase (Table 3).

Finally, strong decompression during amphibolite-facies conditions is characterized by the breakdown of clinopyroxene (Fig. 15 D) and the formation of amphibole due to hydration. Because of decreasing pressure, the X_{Mg} ratio in amphibole also decreases, and the formation of poikilitic garnet and albite-rich plagioclase in metapelites occurred at lower amphibolite- and higher greenschist-facies conditions (Fig. 2A; Tables 3, 6, 7; Supplement Table 3).

6.3. Summary of the P–T loop

The constructed *P–T* loop (Fig. 15D) for the Songea rocks can be subdivided into 5 segments: *Segment (i)* represents the prograde *P–T* path, document by relics of orthopyroxene, garnet and/or garnet profiles of prograde garnet due to crustal thickening (Grt I; Figs. 2F; 3C, D). *Segment (ii)* reflects peak UHT granulite-facies metamorphism at *T* ~1050 °C and *P* up to ~12 kbar (Figs. 8B, 9A; 10B, C). *Segment (iii)* is characterized by strong decompression as seen in the formation of orthopyroxene and plagioclase symplectites, characteristic of UHT metamorphism (Figs. 2D, E). *Segment (iv)* is considered to reflect formation of garnet coronas and represents the transition from granulite- to amphibolite-facies metamorphism (Figs. 2D, F, G). *Segment (v)* signifies strong decompression during amphibolite-facies conditions, seen in the formation of poikilitic garnet and large amphiboles (Fig. 2A).

6.4. Comparison with other granulite-facies areas in the Mozambique belt

Limited exposure of basement rocks within the Mozambique belt of East Africa and Madagascar, with large areas being covered by younger rocks, makes it difficult to compare and correlate different areas with the aim to reconstruct the evolutionary history of the entire region. Geochronological, isotopic and petrological studies were undertaken in various parts of the MB (see summaries and references in Bingen et al., 2009; Collins, 2006; Giese et al., 2011; Jöns and Schenk, 2011; Kröner et al., 1997, 2000, 2001, 2003; Sommer et al., 2003, 2005a,b, 2008; Thomas et al., 2009; Tucker et al., 2011). The following section compares these data with the petrological, geothermobarometric and geochronological data of this study (for names of localities see Fig. 1).

The eastern part of Tanzania (Pare/Usambara/Uluguru/Mahenge Mountains) and SE Kenya (Taita/Sagala Hills, Kasigau) are characterized by granulite-facies metamorphism showing peak metamorphic temperatures and pressures in the range of ~800 °C and 11–13 kbar (Appel et al., 1998; Coolen et al., 1982; Sommer et al., 2003, 2008). This suggests that a large crustal section now exposed was once buried to 35–40 km depth. Most petrological data from eastern Tanzania are compatible with a clockwise *P–T* path for both prograde and retrograde sections. Garnet zonation patterns as well as mineral ages using various isotopic systems with different closure temperatures indicate a slow cooling and exhumation history (Möller et al., 2000).

The rocks of the Songea area do not seem to fit into this uniform pattern of granulites in Tanzania. First, the recorded *P–T* path for Songea rocks provides evidence for isothermal decompression and isobaric cooling in the same samples, a feature that has so far not been found in other granulite-facies terrains of Tanzania. The peak metamorphic temperature at ~1050 °C is higher than elsewhere in Tanzanian granulites, but temperatures up to ~1050 °C are not uncommon, and UHT conditions were described from numerous localities worldwide (Kelsey, 2008) as, for example, Enderby in Antarctica (Harley, 1989), the Namaqua Metamorphic Province in South Africa (Waters, 1989), the Limpopo belt in South Africa (Tsunogae and van Reenen, 2006), the Eastern Ghats belt of India (Sengupta et al., 1999), the North China Craton (Santosh et al., 2007; Zhang et al., 2012), and Pan-African terranes of Brazil and West Africa (Brown, 2006). However, lower *P–T* estimates as exemplified from samples in the vicinity of Songea were also observed in southern Malawi and northern Mozambique. Andreoli (1984) and Kröner et al. (2001) described granulite-facies charnockitic gneisses, biotite-hornblende granulites and migmatic gneisses in southern Malawi where metamorphic conditions were found to be 800–900 °C and ~9.5 kbar. Some granulites were described to have equilibrated at higher *P–T* conditions of ~900 °C and 12 to 15 kbar in southernmost Malawi (Andreoli and Hart, 1990).

The Precambrian basement of northern Mozambique mainly consists of high-grade gneisses, granulites and migmatites, and new data on the geological evolution, geochemistry, and geochronology were reported by Bingen et al. (2009), Boyd et al. (2010), Macey et al. (2010), Thomas et al. (2010), and Ueda et al. (2012).

There are a several smaller continental blocks that were involved in the Neoproterozoic to early Cambrian accretion and collision history of the Mozambique belt. All these led to specific tectono-metamorphic events that occurred at various places and at different times, finally leading to formation of Gondwana (Collins, 2006; Collins and Pisarevsky, 2005; Collins and Windley, 2002).

Geochronological data for almost all the above areas document two age ranges for the peak of high-grade metamorphism: (a) 549–571 Ma in southern Malawi, Madagascar and Sri Lanka, probably correlating with the collision of India with East Africa, and (b) 615–650 Ma in eastern Tanzania (Pare/Usambara/Uluguru/Mahenge Mts.), southern Tanzania, northern Mozambique and western Madagascar (see Table 2). Protolith zircon ages define four groups: (a) Archaean ages of 2.5 to 2.9 Ga in Tanzania and central Madagascar (Collins et al., 2012; Sommer et al., 2003, 2005a,b) (b) Palaeoproterozoic ages of 1.7 to 2.0 Ga in east-central Tanzania (Collins et al., 2004; Muhongo et al., 2001; Reddy et al., 2003; Sommer et al., 2003, 2005a,b; Vogt et al., 2006), (c) Mesoproterozoic ages of 1.0 to 1.3 Ga in southern Tanzania (Kröner et al., 2003), southern Malawi (Kröner et al., 1997), northern Mozambique (Kröner et al., 1997) and central Madagascar (Tucker et al., 2011), and (d) Neoproterozoic ages of ~720–820 in all terranes (Kröner, 2001; Bingen et al., 2009) (Supplement Table 1).

Late Mesoproterozoic to earliest Neoproterozoic granitoid emplacement ages in the Songea area (1027 ± 13, 1158 ± 32, 1192 ± 0.6 Ma) are documented from three of our samples and are similar to isolated granite ages recognized in the Masasi area some 450 km farther E (Kröner et al., 2003). Similar emplacement ages were found in southern Malawi (Kröner et al., 2001) and are common in northern Mozambique and in central Madagascar (Cox et al., 2004; Kröner et al., 2001; Macey et al., 2010; Thomas et al., 2010; Tucker et al., 2011). The significance of these ages is uncertain, but maybe they reflect a connection with the Irumide belt of Zambia (De Waele et al., 2003), but this inference is purely speculative. One Songea granite is significantly younger at 730 ± 0.9 Ma and belongs to the Neoproterozoic age group as also reported elsewhere in the MB of Tanzania, southern Malawi, northern Mozambique and southwest Madagascar (Collins et al., 2012). This magmatic activity may reflect the beginning of subduction of the Mozambique ocean and the development of an Andean-type magmatic arc during convergence between East and West Gondwana (Kröner et al., 2000). However, the existence of East and West Gondwana as separated blocks was superseded and replaced by a Neoproterozoic world, consisting of a number of smaller continents (Collins and Pisarevsky, 2005).

We have not found metamorphic zircons in the Songea samples. Therefore, the peak of granulite-facies metamorphism in this area remains undated. Similar rocks in the Masasi area (Fig. 1A) show metamorphic ages of ~640 Ma (Kröner et al., 2003; Sommer et al., 2003, 2005a). Since no *P–T* estimates for the Masasi rocks are available, it is difficult to directly apply these ages to the Songea area. However, since other granulite-facies areas in Tanzania show similar metamorphic ages and are characterized by slightly higher pressures but lower temperatures (~800 °C, 10–13 kbar), it is likely that the Masasi area also underwent these metamorphic conditions. We therefore conclude that the time of metamorphism in the Songea area was in the same age range as in other areas of Tanzania.

7. Conclusions

Petrological data constrain a precise prograde and retrograde *P–T* loop by means of thermomerty, barometry, *P–T* pseudosections, computed mineral chemical compositions compared with EPMA analyses, volumetric mineral calculations as well as observed reaction textures in granulite-facies rocks and their retrograded equivalents in the Songea area of SW Tanzania. Peak temperatures of up to ~1050 °C and peak pressures of up to ~12 kbar were attained along a five-segment *P–T* path. First, increasing *P–T* conditions are documented by garnet growth (Grt I) due to continent–continent collision and crustal thickening. After reaching peak metamorphic conditions at ~1050 °C and ~12 kbar, isothermal decompression and the formation of orthopyroxene–plagioclase-bearing symplectites occurred due to the consumption of garnet caused by orogenic collapse (Fig. 15D). After the symplectite phase at ~860 °C and ~6.5 kbar, a strong increase in pressure and the formation of garnet (Grt II) is observed, followed by isobaric cooling (Figs. 15A, D). Near-isobaric cooling led to new growth of garnet as coronas around orthopyroxene and Fe–Ti-oxides. The observed texture of an orthopyroxene core and a small clinopyroxene rim, followed by pronounced quartz and garnet coronas, can be explained by volumetric and stoechiometric balancing of the relevant reactions. The formation of garnet coronas probably occurred due to the injection of hot asthenospheric material, which is typical of magmatic underplating. Finally, strong isothermal decompression during amphibolte-facies conditions is seen in the formation of poikilitic garnet and albite-rich plagioclase in the investigated metapelites (Fig. 15D).

Differences in *P–T* conditions and the uncertain age of metamorphism in the Songea rocks preclude a direct comparison and interpretation of the Songea *P–T*-path with those of other terrains in the Mozambique belt. Appel et al. (1998) presented an anticlockwise *P–T*-path for the Usambara/Pare/Uluguru Mts. and interpreted this as evidence for magmatic underplating/overloading. In contrast, the *P–T* paths of Sommer et al. (2003) and this study indicate clockwise prograde metamorphism, followed by strong isothermal decompression and near-isobaric cooling and ending by isothermal decompression under amphibolite-facies conditions. This path is compatible with continental collision, followed by orogenic collapse and associated rifting and the emplacement of post-tectonic granites and pegmatites. On the other hand, one could also argue for two episodes of continental collision, one at granulite-facies and the other at amphibolite-facies conditions. Evidence for an amphibolite-facies collision event is still insufficient and should be the aim of future investigations.

Emplacement ages of ~1027, ~1032 and ~1158 Ma for the magmatic precursor rocks in the Songea area are similar to those in southern Tanzania, southern Malawi and northern Mozambique, but their tectonic setting is uncertain. Although broadly time-equivalent with the Irumide event in Zambia (De Waele et al., 2003) a direct connection with this orogene is speculative. The age of ~770 Ma may reflect the time of UHT metamorphism caused by orogenic collapse and subsequent emplacement of hot asthenospheric material at the base of the continental crust. UHT metamorphic conditions are reported here for the first time from granulites in southern Tanzania. The age of ~730 Ma is likely to reflect the beginning of convergence between Tanzania and SW Madagscar and may be indicative of arc formation at the margin of the Mozambique ocean, eventually leading to ocean closure and collision of East and West Gondwana.

Supplementary data to this article can be found online at http://dx.doi.org/10.1016/j.lithos.2013.02.014.

Acknowledgements

This project was financially supported by Deutsche Forschungsgemeinschaft (DFG) through grant KR 590/72 to A.K. A.K. also acknowledges laboratory facilities in the Max-Planck-Institute für Chemie in Mainz. Zircon analyses of sample Tz 00/15 were performed on the Sensitive High Resolution Ion Microprobe (SHRIMP II) operated by a consortium consisting of Curtin University of Technology, the Geological Survey of Western Australia and the University of Western Australia with the support of the Australian Research Council. Zircons of sample Tz 00/18 were analyzed on the SHRIMP RG of USGS/Stanford

University, USA, and H. S. thanks Joe Wooden for technical advice during analysis and data evaluation. The authors thank Nora Grosschopf for assistance with the microprobe in the Department of Geosciences, Mainz University. Christoph Hauzenberger is acknowledged for providing RFA and microprobe analyses and the microphotographs of Fig. 2. We thank Sospeter Muhongo for organizing logistic support during fieldwork in 2000 and 2001. Finally, we are grateful to M. Scambelluri for editorial handling of the manuscript and A. Collins and an anonymous reviewer for constructive reviews that led to considerable improvement of the manuscript. This is a contribution to the Mainz Geocycles Project.

Appendix A. Analytical methods

Thirty-five thin sections of metapelite, granitic gneiss, migmatite as well as charnockitic gneiss were investigated by transmitted light microscopy and electron microprobe (EMP)/ scanning electron microscope (SEM). Sample locations are shown in Fig. 1B. Mineral analyses were carried out using a JEOL 8900 Superprobe (Mainz) and a JEOL 6310 SEM equipped with a LINK ISIS energy dispersive system and a MICROSPEC wavelength dispersive system (Graz). Standard analytical conditions for silicates were set to an accelerating voltage of 15 kV and 12 nA (JEOL Superprobe) and 5 nA (JEOL SEM) sample current. Matrix corrections for silicates were made using the ZAF procedure. Natural mineral standards were used for calibration. The detection limits in these routine analyses varied from 0.05 to 0.1 wt. % for the Mainz JEOL Superprobe. Geothermobarometric calculations were made with the software package PERPLEX (Connolly, 1990).

Approximately 5 kg of each sample were crushed in Mainz for zircon geochronology, using a jaw crusher and steel roller mill. The crushed material was sieved and fed over a Wilfley table, and a zircon-rich heavy mineral fraction was produced using a Frantz magnetic separator and heavy liquids. Zircons for evaporation and SHRIMP analysis were then handpicked under a binocular microscope. Representative zircons of each sample were mounted in epoxy resin and sectioned approximately in half for cathodoluminescence (CL) imaging to recognize inherited cores and overgrowth patterns (e.g., Hanchar and Miller, 1993; Vavra, 1990). Reconnaissance CL imaging was undertaken on a JEOL 6400 scanning electron microscope (SEM) in the Center for Microscopy and Microanalyis at the University of Western Australia, Perth, operating at 15 kV accelerating voltage and 5 nA beam current.

Single grains were handpicked after optical inspection and analyzed by the evaporation method (Kober, 1986, 1987) using a technique described by Kröner and Hegner (1998). During the course of this study we repeatedly analyzed homogeneous zircon fragments from the Phalaborwa Complex, South Africa, our internal standard. Conventional U–Pb analysis of six separate grain fragments yielded a 207Pb/206Pb age of 2052.2 ± 0.8 Ma (2σ) (W. Todt, unpubl. data), whereas the mean 207Pb/206Pb ratio for 19 fragments, evaporated individually over a period of 12 months, is 0.126634 ± 0.000026 (2σ error of the population), corresponding to an age of 2051.8 ± 0.4 Ma (error 0.2%), identical to the U–Pb age.

Single zircons of sample Tz 00/15 were handpicked and mounted in epoxy resin for SHRIMP II analysis, together with chips of the Perth Consortium zircon standard CZ3. The handling procedure is described in Kröner et al. (1999). Isotopic analyses were performed on the Perth Consortium SHRIMP II ion microprobe, using 7 mass-scans per analysis. Single zircons of sample Tz 00/18 were analyzed on the USGS/ Stanford University SHRIMP RG together with standard RG6, calibrated against Canberra standard SL13, and using 6 mass-scans per analysis The analytical procedures for both SHRIMP instruments are described in Compston et al. (1992), Claoué-Long et al. (1995), and Nelson (1997). SHRIMP data reduction was performed using the Canberra and Perth in-house software programs Prawn 5, Plonk 4.2 and WALLEAD 2.6.

References

Andersen, D.J., Lindsley, D.H., 1988. Internally consistent solution models for Fe–Mg–Mn–Ti oxides: Fe–Ti oxides. American Mineralogist 73, 714–726.
Andersen, D.J., Lindsley, D.H., Davidson, P.M., 1993. QUILF: a Pascal program to assess equilibria among Fe–Mg–Mn–Ti oxides, pyroxenes, olivine, and quartz. Computers & Geosciences 19, 1333–1350.
Andreoli, M.A.G., 1984. Petrochemistry, tectonic evolution and metasomatic mineralization of Mozambique belt granulites from S. Malawi and Tete, Mozambique. Precambrian Research 25, 161–186.
Andreoli, M.A.G., Hart, R.J., 1990. Metasomatized granulites and eclogites of the Mozambique Belt: implications for mantle devolatilization. In: Herbert, H.K., Ho, S.E. (Eds.), Conference on stable isotopes and fluid processes in mineralization: The University of Western Australia, Publication, 23, pp. 121–140.
Appel, P., Möller, A., Schenk, V., 1998. High-pressure granulite facies metamorphism in the Pan-African Belt of eastern Tanzania; P–T–t evidence against granulite formation by continent collision. Journal of Metamorphic Geology 16, 491–509.
Berman, R.G., Arranowich, L.Y., 1996. Optimized standard state and solution properties of minerals I. Model calibration for olivine, orthopyroxene, cordierite, garnet, and ilmenite in the system FeO–MgO–CaO–Al_2O_3–TiO_2–SiO_2. Contributions to Mineralogy and Petrology 126, 1–24.
Bingen, B., Jacobs, J., Viola, G., Henderson, I.H.C., Skar, Ø., Boyd, R., Thomas, R.J., Solli, A., Key, R.M., Daudi, E.X.F., 2009. Geochronology of the Precambrian crust in the Mozambique belt in NE Mozambique, and implications for Gondwana assembly. Precambrian Research 170, 231–255.
Boyd, R., Nordgulen, Ø., Thomas, R.J., Bingen, B., Bjerkgard, T., Grenne, T., Henderson, I., Melezhik, V.A., Often, M., Sandstad, J.S., Solli, A., Tveten, E., Viola, G., Key, R.M., Smith, E., Gonzalez, E., Hollick, L.H., Jacobs, J., Jamal, D., Motuza, G., Bauer, W., Daudi, E., Feitito, P., Manhica, V., Moniz, A., Rosse, D., 2010. The geology and geochemistry of the East African orogen in Northeastern Mozambique. South African Journal of Geology 113, 87–129.
Brown, M., 2006. Styles of orogenesis at the dawn of the Paleozoic era. 33rd International Geological Congress, Oslo, Norway (Abstract CD-ROM MPN-06).
Bucher, K., Frost, R.B., 2006. Fluid transfer in high-grade metamorphic terrains intruded by anorogenic granites: the Thor Range, Antarctica. Journal of Petrology 47, 567–593.
Bucher, K., Grapes, R., 2011. Petrogenesis of Metamorphic Rocks. Springer-Verlag, Berlin Heidelberg.
Claoué-Long, J.C., Compston, W., Roberts, J., Fanning, C.M., 1995. Two Carboniferous ages; a comparison of SHRIMP zircon dating with conventional zircon ages and $^{40}Ar/^{39}Ar$ analysis. SEPM (Society for Sedimentary Geology) Special Publication 54, 3–21.
Collins, A.S., 2006. Madagascar and the amalgamation of Central Gondwana. Gondwana Research 9, 3–16.
Collins, A.S., Pisarevsky, S.A., 2005. Amalgamating eastern Gondwana: the evolution of the Circum-Indian Orogens. Earth-Science Reviews 71, 229–270.
Collins, A.S., Windley, B.F., 2002. The tectonic evolution of central and northern Madagascar and its place in the final assembly of Gondwana. Journal of Geology 110, 325–339.
Collins, A.S., Reddy, S.M., Buchan, C., Mruma, A., 2004. Temporal constraints on Palaeoproterozoic eclogite formation and exhumation (Usagaran Orogen, Tanzania). Earth and Planetary Science Letters 224, 175–192.
Collins, A.S., Kinny, Peter D., Razakamanana, T., 2012. Depositional age, provenance and metamorphic age of metasedimentary rocks from southern Madagascar. Gondwana Research 21, 353–361.
Compston, W., Williams, I.S., Kirschvink, J.L., Zhang, Z., Ma, G., 1992. Zircon U–Pb ages for the Early Cambrian time scale. Journal of the Geological Society of London 149, 171–184.
Connolly, J.A.D., 1990. Multivariable phase-diagrams — an algorithm based on generalized thermodynamics. American Journal of Science 290, 666–718.
Connolly, J.A.D., 2005. Computation of phase equilibria by linear programming: a tool for geodynamic modeling and its application to subduction zone decarbonation. Earth and Planetary Science Letters 236, 524–541.
Coolen, J.J.M.M.M., Priem, H.N.A., Verdurmen, E.A.T., Verschure, R.H., 1982. Possible zircon U–Pb evidence for Pan-African granulite-facies metamorphism in the Mozambique Belt of southern Tanzania. Precambrian Research 17, 31–40.
Cox, R., Coleman, D.S., Chokel, C.B., DeOreo, S.B., Wooden, J.L., Collins, A.S., De Waele, B., Kröner, A., 2004. Proterozoic tectonostratigraphy and paleogeography of central Madagascar derived from detrital zircon U–Pb age populations. Journal of Geology 112, 379–399.
Dale, J., Powell, R., White, R.W., Elmer, F.L., Holland, T.J.B., 2000. A thermodynamic model for Ca–Na clinoamphiboles in Na2O–CaO–FeO–MgO–Al2O3–SiO2–H2O–O for petrological calculations. Journal of Metamorphic Geology 23, 771–791.
De Waele, B., Wingate, M.T.D., Fitzsimons, I.C.W., Mapani, B.S.E., 2003. Untying the Kibaran knot: A re-assessment of Mesoproterozoic correlations in southern Africa based on SHRIMP U–Pb data from the Irumide belt. Geology 31, 509–512.
De Waele, B., Liégeois, J.P., Nemchin, A.A., Tembo, F., 2006. Isotopic and geochemical evidence of proterozoic episodic crustal reworking within the irumide belt of south-central Africa, the southern metacratonic boundary of an Archaean Bangweulu Craton. Precambrian Research 148, 225–256.
Fritz, H., Tenczer, V., Hauzenberger, C., Wallbrecher, E., Hoinkes, G., 2005. Central Tanzanian tectonic map: a step forward to decipher Proterozoic structural events in the East African Orogen. Tectonics 24, TC6013. http://dx.doi.org/10.1029/2005TC001796.
Fritz, H., Tenczer, V., Hauzenberger, C., Wallbrecher, E., Muhongo, S., 2009. Hot granulite nappes — Tectonic styles and thermal evolution of the Proterozoic granulite belts in East Africa. Tectonophysics 477, 160–173.

Frost, R.B., Lindsley, D.H., 1992. Equilibria among Fe-Ti oxides, pyroxenes, olivine, and quartz: Part II. Application. American Mineralogist 77, 1004–1020.
Fuhrman, M.L., Lindsley, D.H., 1988. Ternary-feldspar modeling and thermometry. American Mineralogist 73, 201–215.
Giese, J., Berger, A., Schreurs, G., Gnos, E., 2011. The timing of the tectono-metamorphic evolution at the Neoproterozoic–Phanerozoic boundary in central southern Madagascar. Precambrian Research 185, 131–148.
Hanchar, J.M., Miller, C.F., 1993. Zircon zonation patterns as revealed by cathodoluminescence and backscattered electron images: implications for interpretation of complex crustal history. Chemical Geology 110, 1–13.
Harley, S.L., 1989. The origins of granulites: a metamorphic perspective. Geological Magazine 126, 215–247.
Harpum, J.R., 1970. Summary of the Geology of Tanzania. Geological Survey of Tanzania, Memoir, 1, p. 58.
Hepworth, J.V., 1972. The Mozambique orogenic belt and its foreland in northeast Tanzania; a photogeologically-based study. Journal of the Geological Society of London 128, 461–500.
Holland, T.J.B., Powell, R., 1998. An internally consistent thermodynamic data set for phases of petrological interest. Journal of Metamorphic Geology 16, 309–343.
Holmes, A., 1951. The sequence of pre-Cambrian orogenic belts in south and central Africa. In: Sandford, K.S., Blondel, F. (Eds.), 18th International Geological Congress, London Part XXIV, pp. 254–269.
Hoskin, P.W.O., Black, L.P., 2000. Metamorphic zircon formation by solid-state recrystallization of protolith igneous zircon. Journal of Metamorphic Geology 18, 423–439.
Jacobs, J., Fanning, C.M., Henjes-Kunst, F., Olesch, M., Paech, H.-J., 1998. Continuation of the Mozambique belt into East Antarctica: Grenville age metamorphism and polyphase Pan-African high grade events in central Dronning Maud Land. Journal of Geology 106, 385–406.
Johnson, P.R., Andresen, A., Collins, A.S., Fowler, A.R., Fritz, H., Ghebreab, W., Kusky, T., Stern, R.J., 2011. Late Cryogenian–Ediacaran history of the Arabian–Nubian Shield: A review of depositional, plutonic, structural, and tectonic events in the closing stages of the northern East African Orogen. Journal of African Earth Sciences 61, 167–232.
Jöns, N., Schenk, V., 2011. The ultrahigh temperature granulites of southern Madagascar in a polymetamorphic context: implications for the amalgamation of the Gondwana supercontinent. European Journal of Mineralogy 23, 127–156.
Kelsey, D.E., 2008. On ultrahigh-temperature crustal metamorphism. Gondwana Research 13, 1–29.
Kober, B., 1986. Whole-grain evaporation for $^{207}Pb/^{206}Pb$-age investigations on single zircons using a double-filament thermal ion source. Contributions to Mineralogy and Petrology 93, 482–490.
Kober, B., 1987. Single-zircon evaporation combined with Pb + emitter-bedding for $^{207}Pb/^{206}Pb$-age investigations using thermal ion mass spectrometry, and implications to zirconology. Contributions to Mineralogy and Petrology 96, 63–71.
Kröner, A., 2001. The Mozambique belt of East Africa and Madagascar: significance of zircon and Nd model ages for Rodinia and Gondwana supercontinent formation and dispersal. South African Journal of Geology 104, 151–166.
Kröner, A., Hegner, E., 1998. Geochemistry, single zircon ages and Sm–Nd systematics of granitoid rocks from the Góry Sowie (Owl) Mts., Polish West Sudetes: evidence for early Palaeozoic arc-related plutonism. Journal of the Geological Society of London 155, 711–724.
Kröner, A., Jaeckel, P., Williams, I.S., 1994. Pb-loss patterns in zircons from a high-grade metamorphic terrain as revealed by different dating methods: U–Pb and Pb–Pb ages for igneous and metamorphic zircons from northern Sri Lanka. Precambrian Research 66, 151–181.
Kröner, A., Sacchi, R., Jaeckel, P., Costa, M., 1997. Kibaran magmatism and Pan-African granulite metamorphism in northern Mozambique: single zircon ages and regional implications. Journal of African Earth Sciences 25, 467–484.
Kröner, A., Windley, B.F., Jaeckel, P., Brewer, T.S., Razakamanana, T., 1999. New zircon ages for Precambrian granites, gneisses and granulites from central and southern Madagascar; significance for correlations in East Gondwana. Journal of the Geological Society of London 156, 1125–1135.
Kröner, A., Hegner, E., Collins, A.S., Windley, B.F., Brewer, T.S., Razakamanana, T., 2000. Age and magmatic history of the Antananarivo block, central Madagascar, as derived from zircon geochronology and Nd isotopic sytematics. American Journal of Science 300, 251–288.
Kröner, A., Willner, A.P., Hegner, E., Jaeckel, P., Nemchin, A., 2001. Single zircon ages, PT evolution and Nd isotopic systematics of high-grade gneisses in southern Malawi and their bearing on the extent of the Mozambique belt into southern Africa. Precambrian Research 109, 257–291.
Kröner, A., Muhongo, S., Hegner, E., Wingate, M.T.D., 2003. Single zircon geochronology and Nd isotopic systematics of Proterozoic high-grade rocks from the Mozambique belt of southern Tanzania (Masasi area): implications for Rodinia and Gondwana assembly. Journal of the Geological Society of London 160, 745–757.
Leake, B.E., Wooley, A.R., Arps, C.E.S., Birch, W.D., Gilbert, M.C., Grice, J.D., Hawthorne, F.C., Kato, A., Kisch, H.J., Krivovichec, V.G., Linthout, K., Laird, J., Mandarino, J., Maresch, W.V., Nickel, E.H., Rock, N.M.S., Schumacher, J.C., Smith, D.C., Stephenson, N.C.N., Ungaretti, L., Whittaker, E.J.W., Youzhi, G., 1997. Nomenclature of amphiboles; report of the Subcommittee on Amphiboles of the International Mineralogical Association Commission on New Minerals and Mineral Names. European Journal of Mineralogy 9, 623–651.
Lindsley, D.H., Frost, R.B., 1992. Equilibria among Fe–Ti oxides, pyroxenes, olivine, and quartz: Part I. Theory. American Mineralogist 77, 987–1003.
Maboko, M.A.H., 2000. Nd and Sr isotopic investigation of the Archean-Proterozoic boundary in north eastern Tanzania: constraints on the nature of Neoproterozoic tectonics in the Mozambique belt. Precambrian Research 102, 87–98.
Maboko, M.A.H., Nakamura, E., 1996. Nd and Sr isotopic mapping of the Archaean-Proterozoic boundary in southeastern Tanzania using granites as probes for crustal growth. Precambrian Research 77, 105–115.
Macey, P.H., Thomas, R.J., Grantham, G.H., Ingram, B.A., Jacobs, J., Armstrong, R.A., Roberts, M.P., Bingen, B., Hollick, L., de Kock, G.S., Viola, G., Bauer, W., Gonzales, E., Bjerkgård, T., Henderson, I.H.C., Sandstad, J.S., Cronwright, M.S., Harley, S., Solli, A., Nordgulen, Ø., Motuza, G., Daudi, K., Manhica, V., 2010. Mesoproterozoic geology of the Nampula Block, northern Mozambique: tracing fragments of Mesoproterozoic crust in the heart of Gondwana. Precambrian Research 182, 124–148.
Möller, A., Mezger, K., Schenk, V., 2000. U–Pb dating of metamorphic minerals: pan-African metamorphism and prolonged slow cooling of high pressure granulites in Tanzania, East Africa. Precambrian Research 104, 123–146.
Muhongo, S., 1994. Neoproterozoic collision tectonics in the Mozambique belt of East Africa: evidence from the Uluguru Mountains, Tanzania. Journal of African Earth Sciences 19, 153–168.
Muhongo, S., 1999. Anatomy of the Mozambique belt of eastern and southern Africa: evidence from Tanzania. Gondwana Research 2, 369–375.
Muhongo, S., Kröner, A., Nemchin, A.A., 2001. Single zircon evaporation and SHRIMP ages for granulite-facies rocks in the Mozambique Belt of Tanzania. Journal of Geology 109, 171–189.
Nelson, D.R., 1997. Compilation of SHRIMP U–Pb zircon geochronology data, 1996. Geological Survey of Western Australia, Record 1997/2. (189 pp.).
Newton, R.C., Navrotsky, A., Wood, B.J., 1981. Thermodynamics of Minerals and Melts. Springer, New York.
Pant, N.C., Kundu, A., D'Souza, M.J.D., Saika, A., 2012. Petrology of the Neoproterozoic granulites from Central Dronning Maud Land, East Antarctica - Implications for southward extension of East African Orogen (EAO). Precambrian Research 227, 389–408.
Pinna, P., 1995. On the dual nature of the Mozambique Belt, Mozambique to Kenya. Journal of African Earth Sciences 21, 477–480.
Pinna, P., Muhongo, S., Boniface, A.M., Le Goff, E., Deschamps, Y., Ralay, F., Milesi, J.P., 2004. Geology and Mineral Map of Tanzania. 20th Colloquium of African Geology.
Quennell, A.M., McKinlay, A.C.M., Aitken, W.G., 1956. Summary of the geology of Tanganyika. Geological Survey of Tanganyika, Memoir, 1 (264 pp.).
Reddy, S.M., Collins, A.S., Mruma, A., 2003. Complex high-strain deformation in the Usagaran Orogen, Tanzania: structural setting of Palaeoproterozoic eclogites. Tectonophysics 375, 101–123.
Reddy, S.M., Collins, A.S., Buchan, C., Mruma, A.H., 2004. Heterogeneous excess argon and Neoproterozoic heating in the Usagaran Orogen, Tanzania, revealed by single grain $^{40}Ar/^{39}Ar$ thermochronology. Journal of African Earth Sciences 39, 165–176.
Santosh, M., Tsunogae, T., Li, J.H., Liu, S.J., 2007. Discovery of sapphirine-bearing Mg–Al granulites in the North China Craton: implications for Palaeoproterozoic ultrahigh temperature metamorphism. Gondwana Research 11, 263–285.
Saxena, S.K., Sykes, J., Eriksson, G., 1968. Phase equilibria in the pyroxene quadrilateral. Journal of Petrology 27, 843–852.
Schenk, V., Cornelius, N., Schnieders, I., 2004. Ubendian ultrahigh-temperature metamorphiosm of metapelitic migmatites in the Songea-Mbamba Bay area, southern Tanzania. 20th Colloquium of African Geology, Orléans, France, p. 363 (Abtr.-vol.).
Sengupta, P., Sen, J., Dasgupta, S., Raith, M., Bhui, U.K., Ehl, J., 1999. Ultra-high temperature metamorphism of metapelitic granulites from Kondapalle, Eastern Ghats belt: Implication for the Indo-Antarctic correlation. Journal of Petrology 40, 1065–1087.
Shackleton, R.M., 1986. Precambrian collision tectonics in Africa. In: Coward, M.P., Ries, A.C. (Eds.), Collision tectonics. Blackwell, Oxford, pp. 329–349.
Shackleton, R.M., 1993. Tectonics of the lower crust: a view from the Usambara Mountains, NE Tanzania. Journal of Structural Geology 15, 663–671.
Shackleton, R.M., 1996. The final collision zone between East and West Gondwana: where is it? Journal of African Earth Sciences 23, 271–287.
Silver, L.T., 1969. A geochronological investigation of the anorthosite complex, Adirondack Mountains, New York. In: Isachsen, Y.W. (Ed.), Origin of anorthosite and related rocks: New York Museum and Science Service, Memoir, 18, pp. 233–252.
Sommer, H., Kröner, A., Hauzenberger, C., Muhongo, S., 2003. Metamorphic petrology and zircon geochronology of high-grade rocks from the central Mozambique Belt of Tanzania: crustal recycling of Archean and Palaeoproterozoic material during the Pan-African orogeny. Journal of Metamorphic Geology 21, 915–934.
Sommer, H., Kröner, A., Hauzenberger, C., Muhongo, S., 2005a. Reworking of Archaean and Palaeoproterozoic crust in the Mozambique belt of central Tanzania as documented by SHRIMP zircon geochronology. Journal of African Earth Sciences 43, 447–463.
Sommer, H., Kröner, A., Muhongo, S., Hauzenberger, C., 2005b. SHRIMP zircon ages for post-Usagaran granitoid and rhyolitic rocks from the Palaeoproterozoic terrain of southwestern Tanzania. South African Journal of Geology 8, 247–256.
Sommer, H., Kröner, A., Hauzenberger, C., Muhongo, S., 2008. Isothermal decompression history in the "Western Granulite" terrain, central Tanzania: Evidence from reaction textures in metapelites and trapped fluids. Journal of African Earth Sciences 51, 123–144.
Spooner, C.M., Hepworth, J.V., Fairbairn, H.W., 1970. Whole rock Rb–Sr isotope investigation of some East African granulites. Geological Magazine 107, 511–521.
Stern, R.J., 1994. Arc assembly and continental collision in the Neoproterozoic East African Orogen: implications for the consolidation of Gondwanaland. Annual Reviews of Earth and Planetary Sciences 22, 319–354.
Thomas, R.J., DeWaele, B., Schofield, D.I., Goodenough, K.M., Horstwood, M., Tucker, R., Bauer, W., Annells, R., Howard, K., Walsh, G., Rabarimanana, M., Rafahatelo, J.M., Ralison, A.V., Randriamananjara, T., 2009. Geological evolution of the Neoproterozoic Bemarivo Belt, northern Madagascar. Precambrian Research 172, 279–300.

Thomas, R.J., Jacobs, J., Horstwood, M.S.A., Ueda, K., Bingen, B., Matola, R., 2010. The Mecubúri and Alto Benfica Groups, NE Mozambique: Aids to unraveling ca. 1 and 0.5 Ga events in the East African Orogen. Precambrian Research 178, 72–90.

Thomas, R.J., Roberts, N.M.W., Jacobs, J., Bushid, A.M., Horstwood, M.S.A., Mruma, A., 2013. Structural and geochronological constraints on the evolution of the eastern margin of the Tanzania Craton in the Mpwapwa area, central Tanzania. Precambrian Research. 224, 671–689.

Tsunogae, T., van Reenen, D.D., 2006. Corundum + quartz and Mg-staurolite bearing granulite from the Limpopo Belt, southern Africa: implications for a P–T path. Lithos 92, 576–587.

Tucker, R.D., Roig, J.Y., Macey, P.H., Delor, C., Amelin, Y., Armstrong, R.A., Rabarimanana, M.H., Ralison, A.V., 2011. A new geological framework for south-central Madagascar, and its relevance to the "out-of-Africa" hypothesis. Precambrian Research 185, 109–130.

Ueda, K., Jacobs, J., Thomas, R.J., Kosler, J., Jourdan, F., Matola, R., 2012. Delamination induced late-tectonic deformation and high-grade metamorphism of the Proterozoic Nampula Complex, northern Mozambique. Precambrian Research 196–197, 275–294.

Vavra, G., 1990. On the kinematics of zircon growth and its petrogenetic significance; a cathodoluminescence study. Contributions to Mineralogy and Petrology 106, 90–99.

Vogt, M., Kröner, A., Poller, U., Sommer, H., Muhongo, S., Wingate, M., 2006. Archaean and Palaeoproterozoic gneisses reworked during a Neoproterozoic (Pan-African) high-grade event in the Mozambique belt of East Africa: structural relationships and zircon ages from the Kidatu area, central Tanzania. Journal of African Earth Sciences 45, 139–155.

Waters, D.J., 1989. Metamorphic evidence for the heating and cooling path of Namaqualand granulites. In: Daly, J.S., Cliff, R.A., Yardley, B.W.D. (Eds.), Evolution of metamorphic belts: Geological Society, Special Publications, 43, pp. 357–363.

Zhang, H., Li, J., Liu, S., Li, W., Santosh, M., Wang, H., 2012. Spinel + quartz-bearing ultrahigh-temperature granulites from Xumayao, Inner Mongolia Suture Zone, North China Craton: Petrology, phase equilibria and counterclockwise P–T path. Geoscience Frontiers 3, 603–611.